

Evaluating the resolution of deep mantle plumes in teleseismic traveltime tomography

Ross Maguire¹, Jeroen Ritsema¹, Mickaël Bonnin², Peter E. van Keken³, Saskia Goes⁴

¹Department of Earth and Environmental Sciences, University of Michigan, Ann Arbor, MI, 48109–1005, USA

²Laboratory of Planetology and Geodynamics, CNRS, University of Nantes, Nantes, France

³Department of Terrestrial Magnetism, Carnegie Institution for Science, Washington, DC 20015–1305, USA

⁴Department of Earth Science and Engineering, Imperial College London, London, SW7 2AZ, United Kingdom

Key Points:

- Resolution of deep mantle plume tails is always limited in regional-scale P and S traveltime tomography.
- Optimal resolution of the plume tail requires networks with a wide aperture and dense station spacing.
- Additional imaging improvements are obtained using finite-frequency theory and using SKS traveltimes.

This is the author manuscript accepted for publication and has undergone full peer review but has not been through the copyediting, typesetting, pagination and proofreading process, which may lead to differences between this version and the [Version of Record](#). Please cite this article as doi: [10.1002/2017JB014730](https://doi.org/10.1002/2017JB014730)

Corresponding author: Ross Maguire, romaguir@umich.edu

Abstract

The strongest evidence to support the classical plume hypothesis comes from seismic imaging of the mantle beneath hotspots. However, imaging results are often ambiguous and it is questionable whether narrow plume tails can be detected by present-day seismological techniques. Here, we carry out synthetic tomography experiments based on spectral element simulations of seismic waves with period $T > 10$ s propagating through geodynamically derived plume structures. We vary the source receiver geometry in order to explore the conditions under which lower mantle plume tails may be detected seismically. We determine that wide aperture (4,000 – 6,000 km) networks with dense station coverage ($< 100 - 200$ km station spacing) are necessary to image narrow (< 500 km wide) thermal plume tails. We find that if uncertainties on traveltimes exceed delay times imparted by plume tails (typically < 1 s) the plume tails are concealed in seismic images. Vertically propagating SKS waves enhance plume tail recovery but lack vertical resolution in regions that are not independently constrained by direct S paths. We demonstrate how vertical smearing of an upper mantle low-velocity anomaly can appear as a plume originating in the deep mantle. Our results are useful for interpreting previous plume imaging experiments and guide the design of future experiments.

1 Introduction

Seismic imaging of the structure of mantle plumes and constraining the role of plumes in the dynamics of Earth's remain important research objectives. Estimates of plume heat flux inferred from hotspot swells indicate that plumes carry 5–10% of the Earth's 44 TW of heat [e.g., *Sleep*, 1990]. Plumes may be responsible for the emplacement of large igneous provinces, continental breakup, and mid-plate volcanism (see *Ballmer et al.* [2015] for a review). Over the past two decades seismologists have sought evidence for plumes from estimates of the thermal perturbations of phase boundaries in the transition zone [e.g., *Shen et al.*, 1998; *Li et al.*, 2000; *Schmandt et al.*, 2012] and from tomographic imaging [e.g., *Wolfe et al.*, 1997; *Allen et al.*, 1999; *Montelli et al.*, 2004; *Wolfe et al.*, 2009; *French and Romanowicz*, 2015].

Seismic tomography in particular is a powerful technique to illuminate plumes in the deep mantle and their interactions with large-scale flow and physical boundaries in the mantle transition zone. However, interpreting seismic models remains difficult for several reasons. First, seismic station coverage at hotspots, particularly in oceanic regions,

47 is limited, which inhibits sampling of deep mantle structure with direct P and S waves.
48 Waves that propagate nearly vertically through the mantle, such as SKS, sample the deep
49 structure beneath hotspots but have limited vertical resolution. In regions with low and
50 non-uniform data coverage regularization of the inversion may distort seismic velocity
51 anomalies. The artificial elongation of velocity anomalies along near-vertical teleseismic
52 ray paths complicates estimates of the depth extent of plumes. Second, the delays of seis-
53 mic waves after propagating through narrow plume conduits in the lower mantle may be
54 immeasurably small [e.g., *Hwang et al.*, 2011; *Rickers et al.*, 2012; *Maguire et al.*, 2016].
55 Finite-frequency theory [e.g., *Nolet and Dahlen*, 2000; *Hung et al.*, 2001] accounts for the
56 effects of wave diffraction (i.e., wavefront healing) on traveltimes. However, it is
57 unclear if in practical terms finite-frequency tomography offers higher image resolution
58 compared with ray theoretical tomography when measurement errors and the contributions
59 of shallow structure to traveltimes are relatively large [e.g., *Trampert and Spetzler*,
60 2006].

61 We evaluate how thermal plumes are imaged in teleseismic traveltimes tomography
62 using resolution tests that are commonly applied to assess the potential artifacts in tomo-
63 graphic images [e.g., *Grand*, 1987; *Spakman et al.*, 1989; *Styles et al.*, 2011]. Our models
64 of thermal plumes are based on geodynamic predictions of the temperature structure in
65 the mantle beneath plumes and mineral-physics based estimates of seismic velocities. We
66 calculate the travel time signature of a set of dynamic plume structures using 3D wave-
67 form simulations following our previous work [*Maguire et al.*, 2016]. We invert these
68 'synthetic' data using both ray theory and finite frequency theory following methods us-
69 ing regional-scale teleseismic traveltimes tomography. Our approach is similar to that of
70 *Rickers et al.* [2012] and *Xue et al.* [2015] with the important difference that our plume
71 structures are based on dynamically consistent compressible flow models of mantle plumes
72 that satisfy geodynamic constraints together with a consistent mapping of temperatures to
73 seismic velocity using mineral physics constraints. While plumes in the real Earth may
74 deviate substantially from our idealized models, it is useful to consider geophysically plau-
75 sible plumes since the range of widths, excess temperatures, and velocity perturbations are
76 consistent with our current understanding of mantle dynamics and mineral physics.

77 While it is widely accepted that many hotspots exhibit upper mantle seismic anoma-
78 lies, the debate on the resolvability of lower mantle plume tails continues. Therefore our
79 tests are focused on the imaging of the plume tail in the lower mantle. We do not explore

80 in detail the structure of the plume head in the upper mantle which may be complicated
81 by shearing driven by plate motion and dynamic layering [e.g., *Ballmer et al.*, 2013]. It
82 is our goal to explore how accurately narrow plume tails can be imaged with regional
83 seismic networks, given limited data coverage, inversion regularization, and data uncer-
84 tainty. In synthetic tomography experiments, we vary the source-receiver geometry to de-
85 termine the effects of array aperture and station density on image resolution. We choose
86 regional-scale deployments since the direct phases S and P are ideal phases to image the
87 deep mantle especially when they are recorded by wide-aperture, dense regional networks.
88 We estimate the additional resolving power of SKS waves and assess the value of finite-
89 frequency theory over ray theory. We use Hawaii as our example target and evaluate how
90 well a plume there can be imaged using past and planned offshore seismic deployments in
91 the Pacific Ocean.

92 **2 Methods**

93 **2.1 Numerical simulations of plumes**

94 **2.1.1 Geodynamic modeling**

95 The tested plume structures are based on geodynamic simulations of flow in the
96 Earth using the method previously described by *Maguire et al.* [2016] and *Bossmann and*
97 *van Keken* [2013]. We simulate plumes in a compressible mantle by solving the equations
98 governing conservation of mass, momentum, and energy using the finite-element method
99 in an axisymmetric spherical shell. Plumes are initiated by applying a harmonic perturba-
100 tion to the thermal boundary layer above the CMB.

101 We focus on three plumes with different diameters and strengths (Figure 1). The
102 range of dynamic parameters is summarized in Table 1. The buoyancy flux of the plume
103 tails varies between 1.5 and 3.0 Mg/s, which is consistent with the range of hotspot buoy-
104 ancy fluxes reported in *Sleep* [1990]. The plume structure depends on several factors, in-
105 cluding the temperature contrast across the core-mantle boundary ΔT_{CMB} , the depth de-
106 pendence and temperature sensitivity of viscosity, the thermal expansivity and conductiv-
107 ity, and the Clapeyron slope Γ_{660} of the ringwoodite-bridgmanite transition near a depth
108 of 660 km (abbreviated as the ‘660’ from hereon). We use a temperature- and depth-
109 dependent viscosity $\eta(T, z) = \eta_0(z) \exp(-b(T - T_{ref}))$ which represents a linearization
110 of the Arrhenius viscosity law. We choose b to be in the range of $\ln(10^1)$ to $\ln(10^3)$. The

111 latter value is consistent with olivine under diffusion creep with an activation energy of
112 $E = 300 \text{ kJ mol}^{-1}$. The depth-dependent viscosity profile $\eta_0(z)$ is defined by three layers.
113 In the lower mantle $\eta_0(z) = 10^{22} \text{ Pa s}$. In the upper mantle we reduce the viscosity by
114 a factor of 30 in a number of models. The uppermost 120 km of the mantle represents a
115 high-viscosity lithosphere with $\eta_0(z) = 10^{24} \text{ Pa s}$.

116 Models R1a, R1b, and R1c represent three stages of development of the same dy-
117 namic simulation. After 45 Myr, plume R1a is a starting plume with a head rising in the
118 lower mantle. After 55 Myr, plume R1b has reached the upper mantle and has begun to
119 spread beneath the lithosphere. The plume structure is complex near the 660 because this
120 boundary partially impedes the flow. After 175 Myr, plume R1c has a quasi-steady state
121 structure. Phase boundary effects have dissipated and the plume head has spread com-
122 pletely beneath the lithosphere. Its tail in the lower mantle has a cylindrical structure with
123 a width of about 500 km. R1c is thinner in the asthenosphere by a factor of about two
124 due to the viscosity reduction above 660. Plume R2 has an anomalously wide (about 800
125 km) tail due to the modest temperature dependence of viscosity compared to the other
126 models. Plume model R3, on the other hand, has an anomalously thin (less than 400 km
127 wide) and weak tail because the temperature contrast across the CMB is relatively small
128 at 550 K and the viscosity is strongly temperature dependent ($b = \ln(10^3)$). The heads of
129 plumes R1c and R2 have spread horizontally a significant distance beneath the lithosphere.
130 We artificially truncate them to be no wider than 5 degrees from the plume axis so they
131 do not overwhelm the traveltime delay signal from the tail in the deep mantle.

132 We do not model any thermochemical plumes and therefore ignore the complexities
133 that may arise when chemical entrainment of a dense layer is modeled. *Lin and van Keken*
134 [2006] and *Dannberg and Sobolev* [2015] showed that entrainment of dense eclogitic ma-
135 terial may reduce plume buoyancy and broaden plumes in the lower mantle. In addition,
136 non-peridotitic components could change the amplitude of the seismic anomaly. While
137 plumes R1, R2, and R3 are purely thermal in origin the travel time delays in the plume
138 tails are approximately linear with respect to velocity perturbation [e.g., *Mercerat and No-*
139 *let*, 2013; *Maguire et al.*, 2016]. Therefore our results can provide insight into the resolv-
140 ability of stronger or weaker thermochemical plume tails with similar widths.

2.1.2 Seismic velocity structure of plumes

The calculation of the seismic velocity structure of plumes R1, R2, and R3 in Figure 1 follows the same steps as in *Maguire et al.* [2016]. We assume a constant pyrolytic composition [Workman and Hart, 2005], defined in the NCFMAS system (i.e., in terms of the six oxides Na₂O, CaO, FeO, MgO, Al₂O₃, and SiO₂). Using the code *Perple_X* [Connolly, 2005] and the thermodynamic database of *Stixrude and Lithgow-Bertelloni* [2011], we compute the equilibrium mineral assemblage and the corresponding elastic parameters and density as a function of pressure and temperature. The seismic velocity of the bulk mineral assemblage is the Voigt-Reuss-Hill average of the velocity of each phase. Subsequently, we add the effects of temperature, pressure, and frequency-dependent anelasticity using model Q7g (as in *Maguire et al.* [2016]). The maximum velocity reduction within plume tails is about 4% for shear waves and 2% for compressional waves. *Cobden et al.* [2008] provide further details of the thermodynamic method including sources of uncertainty.

2.2 Seismic modeling

2.2.1 Computation of travel time delays

The Preliminary Reference Earth Model (PREM) [Dziewonski and Anderson, 1981] is our reference seismic structure of the mantle without plumes. We construct seismic structures for plumes R1, R2, and R3 by superposing their velocity perturbations (from Figure 1) on PREM. We note that the choice of reference structure is not an important factor in our analysis given that commonly used 1D Earth models deviate only slightly in the lower mantle. We determine the traveltimes delays of the phases P, S, and SKS using spectral-element method (SEM) waveform simulations. The seismic wavefield is described within each element as an expansion in fourth-order Lagrange polynomials. The SEM waveforms are accurate to wave periods longer than 10 s, corresponding to wavelengths in the lower mantle of 130 km (for P waves) and 80 km (for S waves). In contrast to our previous work [Maguire et al., 2016] which was based on SES3D [Gokhberg and Fichtner, 2016], we use the spectral-element code SPECFEM3D GLOBE [Komatitsch and Tromp, 2002] to simulate the waveforms of core phases.

We analyze synthetic waveforms at teleseismic distances. As an example, Figure 2a shows the ray paths of S and SKS propagating through plume R1c for two events at

172 distances $D = 50^\circ$ (for S) and $D = 100^\circ$ (for SKS) from the plume axis. When the plume
 173 axis is at a distance D of 50° from the event, the S waves at epicentral distances between
 174 60° and 90° cross the plume tail in the lower mantle. The SKS waves traverse the plume
 175 tail more vertically up to an epicentral distance of 110° when the plume–event distance D
 176 is 100° .

177 We calculate traveltime differences for P, S, and SKS between PREM and the 3-D
 178 plume structures by comparing waveform segments centered on P, S, and SKS. The win-
 179 dows are approximately 50 s wide. The seismograms are bandpass filtered between 0.1 Hz
 180 and 0.04 Hz. We consider cross correlation delay times when applying finite frequency to-
 181 mography and onset delay times when applying ray theoretical tomography since the wave
 182 onset is a high-frequency signal of a waveform. We discard measurements for waveforms
 183 affected by the interference between S and SKS near an epicentral distance of 80° .

184 2.2.2 Tomographic inversion

185 We invert travel time delays to estimate P-wave and S-wave structure using either
 186 ray theory (RT) or finite-frequency theory (FF) following the procedures that have been
 187 applied to regional network data [e.g., *Bonnin et al.*, 2014]. The theories provide funda-
 188 mentally different relationships between velocity heterogeneity in the mantle and recorded
 189 traveltime delays. According to RT, the travel time delay is sensitive to wavespeed varia-
 190 tion along the ray path S :

$$191 \delta T = - \int_S \frac{\delta v}{v} ds, \quad (1)$$

192 where v is the absolute seismic velocity and δv is the fractional perturbation relative to
 193 v . In FF, the travel time delay is influenced by seismic structure within a volume V sur-
 194 rounding the ray path:

$$195 \delta T = \int_V K(\mathbf{x}) \delta v dV, \quad (2)$$

196 where the sensitivity kernel $K(\mathbf{x})$ is related to the Fresnel zone.

197 Figures 2b, 2c, and 2d illustrate the cross-sectional form of $K(\mathbf{x})$ for S, P, and SKS
 198 measurements, respectively. S and P kernels are shown for events recorded at an epicentral
 199 distance of 80° and the SKS kernel is shown for an event recorded at epicentral distance
 200 of 100° . The kernels reflect the sensitivity of cross correlation delay time observations to
 waves filtered between $10 \text{ s} < T < 25 \text{ s}$ period. At the wave turning depth, the kernel is
 about 1,000 km wide but the width depends on epicentral distance and wave period. We

201 compute the kernels $K(\mathbf{x})$ for PREM using the paraxial ray approximation introduced by
 202 *Dahlen et al.* [2000]. We ignore the effects of velocity structure on the ray path S and on
 203 the sensitivity kernels $K(\mathbf{x})$ which we expect to be weak for plume tails [e.g., *Mercerat*
 204 *and Nolet*, 2013].

205 The model \mathbf{m} is based on the cubed-Earth parameterization [e.g., *Charl ty et al.*,
 206 2013; *Bonnin et al.*, 2014] and consists of about 3.5×10^6 blocks with horizontal side
 207 lengths between 59–83 km and vertical side lengths between 44–90 km which increase
 208 with depth. The global parameterization accommodates both mantle and core phases at
 209 teleseismic distances. The size of each voxel is small compared to the width of the finite
 210 frequency sensitivity kernels. The distinct 3-D shapes of the kernels are preserved when
 211 projected onto the parameterization [*Chevrot et al.*, 2012].

212 Given the large number of model parameters, we regularize the inversion by apply-
 213 ing norm damping (i.e, the total size of the model) and smoothness damping (i.e., the sec-
 214 ond spatial derivative of the model). We minimize the object function $O(\mathbf{m})$

$$O(\mathbf{m}) = (\mathbf{G}\mathbf{m} - \mathbf{d})^2 + \epsilon_n \mathbf{m}^2 + \epsilon_s (\mathbf{S}\mathbf{m})^2. \quad (3)$$

215 The first term of $O(\mathbf{m})$ represents the data misfit. The second and third terms represent
 216 the model size and the model roughness, respectively. The system matrix \mathbf{G} incorpo-
 217 rates the forward theory, \mathbf{d} is the vector of travel time delays, ϵ_n and ϵ_s are the norm
 218 and smoothness damping parameters, and \mathbf{S} is a smoothness matrix which minimizes the
 219 Laplacian of the model.

220 The data misfit, χ^2 , is defined as

$$\chi^2 = \sum_i^N \frac{(\sum_j G_{ij} m_j - d_i)^2}{\sigma_i^2}, \quad (4)$$

221 where N is the number of data and i and j are the indices of traveltimes delays and model
 222 parameters, respectively. When the model fits the data to within measurement uncertain-
 223 ties, $\chi^2 = N$. We add varying amounts of Gaussian noise to the synthetic delay time data
 224 to approximate random measurement error.

225 We experiment with different values of the measurement uncertainty σ to estimate
 226 preferred models \mathbf{m} . We choose the minimum value for σ of 0.1 s, which is equivalent
 227 to the time step in the waveform simulations. The maximum value of σ is 1.0 s or 10%
 228 of the dominant wave period. It represents a realistic error when the match between ob-

229 served and synthetic waveforms is poor and when the effects on waveforms of the crust,
230 anisotropy, and 3-D heterogeneity in the deep mantle are uncertain.

231 We determine the optimal model, by varying the values of ϵ_s and ϵ_n , while setting
232 their ratio constant ($r = \epsilon_s/\epsilon_n$). Our tests indicate that $r = 5$ provides a suitable balance
233 between smoothness and norm damping and we use this value for all inversions unless
234 otherwise noted. The effect of the choice of regularization parameters is explored in Sec-
235 tion 4.7.

236 Figure 3 shows an example of tradeoff curves used to determine the best fit model
237 for both RT and FF. In both RT and FF the optimal model is near the bend of the trade-
238 off curve, which indicates that error estimates are well constrained. However, for a given
239 variance reduction χ^2/N , FF always leads to a model \mathbf{m} with a larger L2 norm, indicating
240 that FF recovers images of plume structures with higher amplitudes.

241 **3 Network configurations**

242 Seismic network configuration and wave sampling are the key factors determining
243 tomographic image resolution. To understand plume resolution given the practical limi-
244 tations of network design, especially in ocean basins, we conduct tomographic inversions
245 of the synthetic traveltimes data for four different network configurations. We determine
246 the resolution of plumes given (i) ideal data coverage and (ii) incomplete data coverage
247 that is representative of past or newly designed experiments near Hawaii and in the Pacific
248 Ocean.

249 **3.1 Configuration A: large network aperture, small station spacing, and homoge- 250 neous event distribution**

251 An ideal seismic network has a wide aperture with dense station spacing and records
252 earthquakes over a full range of epicentral distances and azimuths. Here, we assume such
253 a network to be a square grid of stations with a width L and station spacing Δx . The
254 events are at distances D between 30° and 120° and at azimuths every 30° (Figure 4a).

255 We vary L and Δx to explore how network aperture and station density affect reso-
256 lution. For the largest and densest grid, when $L = 6,000$ km and $\Delta x = 100$ km the data
257 coverage is optimal, because the inversion results do not improve appreciably if the net-

258 work aperture L is larger or if station spacing Δx is smaller. The largest network consid-
259 ered provides 254,193 paths for P and S.

260 **3.2 Configuration B: the PLUME geometry**

261 The PLUME experiment [Laske *et al.*, 2009; Wolfe *et al.*, 2009] was a comprehensive
262 seismic experiment aimed at imaging the mantle beneath the Hawaiian hotspot. The ex-
263 periment consisted of 67 land and ocean-bottom seismometers on and surrounding Hawaii
264 which were in operation for more than two years. Figure 4b shows the station distribution
265 of the PLUME experiment, following the description of Wolfe *et al.* [2009]. The network
266 aperture is over 1,000 km, with stations typically spaced about 100 km apart. In simu-
267 lating a set of traveltimes, we use earthquake locations from all events greater than M_W
268 6 that occurred during the two-year deployment of the PLUME network at epicentral dis-
269 tances between 30° and 120° . The events are not exactly the same as those used by Wolfe
270 *et al.* [2009], which were selected on the basis of waveform quality, but the azimuthal
271 and distance distributions are similar. The total number of raypaths for P- and S-waves
272 is 5,276.

273 **3.3 Configuration C: wide-aperture linear arrays**

274 The small array aperture of the PLUME experiment limits the imaging of lower
275 mantle beneath Hawaii. Here, we explore how tomographic resolution can be improved
276 if a hypothetical seismic array deployment has a wider aperture and would be operating
277 for a longer time. The deployment consists of three linear arrays which intersect at Hawaii
278 (Figure 4c). The station spacing is $\Delta x = 200$ km, and the length of each array is 50 de-
279 grees. The total number of seismometers is 87. In our test the angles between each limb
280 of the array is 60° and is optimally aligned with regions of relative high seismicity. We
281 consider a five-year deployment and simulate traveltime measurements for all teleseismic
282 earthquakes greater than M_W 6 that have occurred between 2012 and 2017, which pro-
283 vides 50,738 raypaths for P- and S-waves.

284 **3.4 Configuration D: the Pacific Array**

285 The fourth network configuration is based on a conceptual Pacific-wide network
286 called "The Pacific Array" as envisioned by Kawakatsu *et al.* [2016]. The anticipated con-

287 figuration of PA is shown in Figure 4d. The Pacific Array (PA) constitutes "an array of
288 arrays". Each of the 14 sub-arrays is comprised a spiral of 10 stations with an aperture
289 of about 500 km which enables the measurement of surface-wave dispersion to study the
290 structure of the crust and lithosphere across the Pacific. The network as a whole provides
291 improved body-wave coverage of the deep mantle. We assume in our modeling that the
292 PA would have been active for the same 2012–2017 period as the previous configuration.
293 The array provides 62,715 direct body-wave paths over this time span.

294 **4 Results**

295 We first explore the impact of plume tail width on resolution by showing inversion
296 results for each plume structure using the optimal source-receiver configuration. We next
297 illustrate how data coverage and other aspects of the inversion process affect image resolu-
298 tion.

299 **4.1 Plume images for ideal data coverage**

300 Figure 5 shows the resolved images of plumes R1 (at stages a, b, and c), R2, and
301 R3 using FF and RT inversions of S-wave delay times. We use network configuration
302 A shown in Figure 4a with $L = 6,000$ km and $\Delta x = 100$ km and assume that the uncer-
303 tainty in the S-wave traveltimes delays has a Gaussian distribution with a standard devia-
304 tion $\sigma = 0.1$ s. This represents an optimal scenario for a tomographic inversion of tele-
305 seismic traveltimes at a regional network of stations: the network aperture is wide, the
306 station spacing is small, the earthquake distribution is uniform, and the traveltimes mea-
307 surements are precise.

308 Despite the optimal setup, the images derived using both RT and FF reveal the sig-
309 nificant distortions and amplitude loss. The intricate head and stem features of the plume
310 in the upper mantle (e.g., plumes R1b and R1c) or lower mantle (e.g., R1a), the dynamic
311 effects of the 660 on plume ascent, and the thinning of the conduit in the low-viscosity
312 upper mantle above the 660 are unresolved. The velocity anomaly of the plume in the
313 lower mantle is strongly reduced due to wavefront healing and the applied model damp-
314 ing. For the same variance reduction, FF resolves the plume tail in the lower mantle with
315 a higher amplitude than RT. For example, $\delta V_S = -1\%$ in the resolved plume tail of R1b
316 imaged with FF, while is only about -0.2% with RT δV_S .

317 The width of the plume tail is a primary factor in determining the fraction of the
 318 input anomaly recovered. Plume R3 has the thinnest tail (less than 400 km wide) and is
 319 resolved with the greatest amplitude reduction. With FF the tail is imaged with an ampli-
 320 tude $\delta V_S = -0.5\%$, which is only about 25% of the strength of the input structure. With
 321 RT, the shear velocity reduction δV_S in the tail is smaller than 0.1%, which we consider to
 322 be undetectable. The tails of plumes R1b and R1c are slightly wider (about 500 km wide)
 323 and are recovered with greater amplitude. In the lowermost mantle, with FF, the tails of
 324 R1b and R1c are imaged with an amplitude of about $\delta V_S = -1\%$, which is about 30% of
 325 the amplitude of the input structure. In the mid-mantle, R1c is imaged with greater am-
 326 plitude than R1b since the tail of R1b thins slightly near 1500 km depth. With RT, the
 327 tails of R1b and R1c are close to invisible in the lowermost mantle (δV_S of about -0.2%).
 328 The wide plume tail of R2 (diameter of 800 km) is imaged with the highest amplitude.
 329 More than 50% of the initial anomaly is recovered to a depth of 1800 km (imaged ampli-
 330 tude $\delta V_S < -2\%$). Near the base of the mantle the tail diminishes in strength to about
 331 $\delta V_S = -1\%$. The broad lower mantle plume head of R1a is imaged with little ampli-
 332 tude reduction with both FF and RT (about 75% of strength of the input structure), but
 333 the short stem is less accurately recovered.

334 4.2 Effects of network spacing and aperture

335 Image resolution depends on wave path coverage. Networks with dense station spac-
 336 ing offer data redundancy and enable resolution of fine-scale structure. Depth resolution is
 337 best for the network with the widest aperture as teleseismic wave crisscross the mantle at
 338 large range of angles.

339 To illustrate how image resolution depends on network aperture and station density,
 340 we show in Figure 6 the resolved fractional amplitude F with respect to the shear velocity
 341 anomaly in the input model: $F = \delta V_S^{\text{OUT}} / \delta V_S^{\text{IN}}$. For plume R1b and using FF, we deter-
 342 mine F at three depths along the plume axis in the lower mantle. We use network config-
 343 uration A for values of L of 2,000 km, 4,000 km, and 6,000 km and Δx of 100 km, 200
 344 km, and 500 km. The standard deviation of delay time measurement error is $\Delta\sigma = 0.1$ s.

345 Resolution decreases with increasing depth z because data coverage diminishes. For
 346 the smallest width ($L = 2,000$ km), teleseismic S-waves do not cross the plume axis at
 347 depths larger than 2,000 km so $F = 0$ regardless of the station spacing Δx . When $L =$

4,000 km, the plume tail is resolved to over 2,000 km depth. There is a weak signal of plume tail at 2,400 km depth only when the network width is $L = 6,000$ km. However, the narrow plume tail is resolved with a significant amplitude reduction. At 1600 km depth, F in the plume tail is lower than 30% for the widest width L of 6,000 km and the smallest station spacing Δx of 100 km considered. F decreases with increasing station spacing because the data misfit makes a smaller contribution to the object function O (equation 3).

4.3 P-velocity versus S-velocity inversion

Figure 7 shows a comparison between S-wave and P-wave inversions for plume R1c using FF theory. We use configuration A and $L = 6,000$ km, and $\Delta x = 100$ km and assume that the standard deviation of random traveltimes error $\sigma = 0.1$ s. Throughout the lower mantle, S wave inversions recover a larger fraction of the input anomaly than P wave inversions. The velocity anomaly in the lower mantle is about -1.0% for S (30% of the amplitude in the input structure) and -0.3% for P (15% of the amplitude in the input structure).

There are two reasons for the higher amplitudes of S velocity anomalies. First, δV_S is stronger than δV_P in the input structures by about a factor of two due to the greater sensitivity of V_S to temperature. Second, the P-wave has a larger wavelength, a wider Fresnel zone, and is more susceptible to the effects of wavefront healing. Given its wider Fresnel zone, a P-wave is sensitive to structure in the mantle over a broader volume than S-waves and P velocity heterogeneity is imaged with a lower amplitudes. We note that we are comparing inversions of P and S-wave delays calculated in the same frequency band. In practice, P waves may be analyzed at higher frequencies than S waves. If P delays are determined at a period of $T = 5$ s, we expect to recover the same fraction of the plume tail because the sensitivity kernels of P and S would be of comparable size.

4.4 The effect of measurement uncertainty

To test the effect of uncorrelated error in travel time measurements, we invert S-wave delay times with variable amounts of assumed noise. We use configuration A with $L = 6,000$ km and $\Delta x = 200$ km and choose three values for the standard deviation of traveltimes error: $\sigma = 0.1$ s, $\sigma = 0.5$ s, and $\sigma = 1.0$ s. We test the effects for plume R1b using FF.

378 With increasing values of σ , model damping and regularization have higher influ-
379 ence (see equation (3)). This is evident from the comparison of the resolved structure of
380 plume R1b for the three values of σ in Figure 8. When the traveltimes error is smallest
381 (i.e., $\sigma = 0.1$ s), the deep plume tail is resolved with an amplitude of $\delta V_S \approx -1.0\%$. For
382 $\sigma = 0.5$ s, the recovered shear velocity anomaly in the plume tail is δV_S is weaker than
383 -0.2% and the resolved δV_S is smaller than -0.1% for $\sigma = 1.0$ s. These weak anomalies
384 are likely undetectable.

385 4.5 Comparison between networks

386 Figure 9 compares the resolved images of plume R1c for the four network configu-
387 rations discussed in section 4. We assume $\sigma = 0.1$ s and invert the delay times using FF.
388 We invert either the delay time of S (Figure 9; first column) and S with SKS (Figure 9;
389 second column).

390 High data coverage is key for the imaging of the plume tail in the lower mantle. The
391 images obtained using the optimal experiment geometry are shown in the first row of Fig-
392 ure 9 (see also Figure 4). They exhibit signatures of the tail of plume R1c deep into the
393 lower mantle. The shear velocity anomaly δV_S in the plume tail is lower for configuration
394 B (representative of the PLUME network around Hawaii) because the aperture is much
395 smaller and the event distribution is inhomogeneous. When distributing a similar num-
396 ber of stations as in B into wide-aperture linear arrays (configuration C), the imaging of
397 the deep mantle structure is significantly better. The Pacific Array distribution of stations
398 across the Pacific Ocean (configuration D) produces a weak signature of the tail in the
399 lower mantle. However, without dense station coverage the images are missing a clear
400 mantle-wide expression of plume R1c into the upper mantle. We note that resolution in
401 the mid and shallow mantle can be improved by incorporating surface reflections (e.g.,
402 SS) and surface wave constraints.

403 Figure 9 demonstrates also that SKS traveltimes provide resolution of the structure
404 in the lower mantle. For example, for configuration A the shear velocity anomaly δV_S in
405 the plume tail diminishes from about -2.0% at 1,000 km depth to less than -1.0% near
406 the base of the mantle when only S traveltimes delays are inverted. A joint inversion of
407 S and SKS traveltimes delays produces a nearly constant δV_S of -2.0% in the plume tail
408 throughout the lower mantle.

4.6 The resolving power of SKS

Wolfe et al. [2009] concluded that SKS is capable of driving resolution of the deep mantle where direct S-waves are absent. Our results confirm this, as is evident in the second row of Figure 9, which shows R1c imaged with the PLUME network (i.e., configuration B). When inversions are performed using only S (first panel), the plume is not imaged below a depth of 1,000 km. When SKS is included (middle panel), the plume tail is apparent to a depth of 1,800 km.

However, since SKS propagates nearly vertically through the mantle, it is difficult to resolve structure in the upper mantle and lower mantle independently. To illustrate this, plume head in the upper mantle, we compute and invert S and SKS travel time delays for the same plume R1c in which we have set $\delta V_S = 0$ in the lower mantle (Figure 10a). The NW–SE and SW–NE oriented cross sections in Figure 10b and 10c indicate that upper mantle structure is projected into the lower mantle along dominant S and SKS paths. For instance, the steeply dipping anomaly in Figure 10c, labeled X, projects towards a cluster of events in South America at large epicentral distances that produces most of the SKS traveltimes. In Figure 10d the more shallowly dipping anomaly Y has a direction towards the SW, parallel to S-wave paths between Hawaii and Tonga. Similar artifacts towards the NE are missing because only one event in North America contributes to the collection of traveltimes.

4.7 Fast anomalies due to regularization

When data coverage is sparse, regularization artifacts tend to dominate tomographic images. In particular, when strong preference is given to smooth models, artificial high-to-low seismic velocity oscillations may be introduced. Figure 11 shows inversion results for R1b imaged with configuration B, in which a high velocity ring shaped anomaly is introduced surrounding the plume head in the upper mantle. The amplitude of the feature is as large as $\delta V_S = +1.0\%$, and could be misinterpreted as dynamic in origin. The artifact is several hundred km wide in some cases, which is much wider than the blocks used in the model parameterization. A notable gap in the ring anomaly is present NE of Hawaii due to a lack of raypath coverage from North American events. The strength and extent of the artifact depends on the choice of regularization. Figure 11a shows an inversion with $\epsilon_s/\epsilon_n = 50$ (strong preference for smooth models), and 11b shows an inversion with

440 $\epsilon_s/\epsilon_n = 0.02$ (strong preference for small models). In both cases, the fast ring anomaly is
441 present, however it is more prominent when preference is given to smoothness.

442 The tradeoff for minimizing the high velocity artifact (i.e., giving stronger preference
443 to norm damping), is that a smaller fraction of the true strength of the plume is recovered.

444 5 Discussion

445 The Hawaii PLUME network has been one of the most comprehensive experiments
446 for studying the structure the mantle beneath a hotspot. It comprised an array of both on-
447 shore and off-shore seismic instrumentation designed to maximize imaging resolution
448 given the constraints on budget and operational logistics. We have also focused on the
449 PLUME experiment in our analysis to illustrate how the imaging of a plume tail in the
450 deep mantle beneath a regional seismic network is complicated by the limited array aper-
451 ture and inhomogeneous data coverage.

452 Our analysis confirms that the PLUME experiment is capable of imaging deep man-
453 tle structure if traveltimes measurements of SKS are incorporated in the analysis. However,
454 the limited vertical resolution complicates the interpretation of teleseismic traveltimes to-
455 mography images. Seismic structure in lower mantle cannot be resolved independently
456 from structure in the upper mantle from regional network data. Our simple test (shown
457 in Figure 10) illustrates how seismic structure in the upper mantle can be projected into
458 the lower mantle along dominant S and SKS paths particularly towards regions with high
459 seismicity. Steeply elongated anomalies in the lower mantle follow SKS paths to distant
460 earthquakes in South America while more shallowly dipping anomalies extend to nearer
461 earthquakes in the western Pacific. These anomalies are reminiscent of the anomalies re-
462 solved by *Wolfe et al.* [2009].

463 However, we do not dismiss the results from *Wolfe et al.* [2009]. In our experiment
464 using the head structure of plume R1c, the velocity reduction in upper mantle is as high
465 as $\delta V_S = -10\%$, corresponding to a temperature anomaly of $\Delta T = 400$ K, which is likely
466 to be unrealistically high. We predict that the velocity anomalies that are projected from
467 an upper mantle plume expression have rather low amplitude ($\delta V_S = -0.3\%$) which is
468 lower than that recovered in the original PLUME experiment (δV_S of about -0.5% extend-
469 ing into the mid-mantle). While the pattern of smearing is similar between the original

470 experiment and our synthetic analysis, the higher amplitude found in the PLUME experi-
471 ment may well indicate that a true lower mantle plume expression was recovered.

472 Over the course of its deployment the EarthScope USArray covered the entire con-
473 tiguous United States (about 4,000 km wide) with stations typically spaced less than 100
474 km apart. Recent tomographic images using data from USArray [e.g., *Schmandt et al.*,
475 2012; *Porrirt et al.*, 2014; *Burdick et al.*, 2017] have been used to test the hypothesis that
476 the Yellowstone hotspot has a deep mantle plume origin. *Schmandt and Lin* [2014] image
477 a mostly vertical slow velocity anomaly beneath Yellowstone to a depth of about 900 km.
478 *Porrirt et al.* [2014] image a slow wavespeed anomaly to at least the base of the transition
479 zone and potentially deeper, although below the transition zone the anomaly is weakened
480 and tilted. Our results shown in Figure 6 suggest a network comparable to USArray is ca-
481 pable of imaging a plume tail to at least 2000 km depth.

482 The uncertain detection of a plume tail extending into the deep mantle beneath Yel-
483 lowstone could be due to several reasons. First, a plume tail may be absent if Yellowstone
484 volcanism is fed by a shallow source, or if the deep plume source is waning. Second, the
485 plume may be thinner or weaker than those we consider and thus impart smaller travel
486 time delays. Uncertainties of travel time observations due to the influence of heteroge-
487 neous crust may also make imaging the deep plume tail challenging. Additionally, plume
488 dynamics may be complicated by interaction with the sinking Farallon slab [e.g., *Leonard*
489 *and Liu*, 2016].

490 The imaging of small scale structure in the deep mantle can potentially be improved
491 either by using multiple-frequency tomography [e.g., *Sigloch et al.*, 2008], which exploits
492 the frequency dependence of body wave dispersion, or full-waveform inversion (FWI)
493 which uses large portions of the seismic signal at broadband frequencies [e.g., *Rickers*
494 *et al.*, 2013; *French and Romanowicz*, 2015; *Bozdağ et al.*, 2016]. A major challenge of
495 FWI is in distinguishing low-amplitude diffracted arrivals in the coda of main arrivals
496 from crustal scattering. FWI may be particularly useful in regions such as the Pacific
497 Plate surrounding Hawaii where the crust is relatively simple. While FWI may be an im-
498 provement over traveltimes tomography, we argue that the lack of data coverage is still the
499 limiting factor in the imaging of plume tails in the deep mantle. Our analysis here shows
500 that large-scale OBS deployments, while costly, can improve seismic models of the deep
501 mantle and advance the plume debate forward significantly.

6 Conclusions

Traveltime tomography is the most powerful tool to image the structure of the deep mantle but the resolution of small-scale structures such as plume tails is inherently limited. To quantify resolution of thermal plume ascent from the core-mantle boundary, we have investigated how deep-mantle plumes are imaged by teleseismic traveltime tomography using regional networks of seismometers and analytical procedures similar to those commonly applied to real data.

We have explored best-case scenarios for network design and data coverage and deployments based on past and proposed experiments. Our computations of plume formation at the core-mantle boundary and plume ascent through the mantle incorporate realistic constraints on thermodynamic and rheological conditions of the mantle and plume buoyancy flux. We use mineral physics constraints to relate the elevated temperature to wave speed reductions in the plume. We predict the traveltime delays from 3-D spectral element method waveform simulations at periods longer than 10 s and invert them using both ray-theory and finite-frequency theory.

Plume tails are imaged with considerably reduced strengths even under ideal imaging conditions. For wide-aperture, dense networks of stations which have recorded earthquakes at a uniform range of azimuths and epicentral distances, a plume tail in the lower mantle is imaged with an amplitude loss of at least 40%. The strength of the imaged plume tail depends on many factors. We have explored the effects of network aperture, station spacing, data types, delay-time measurement uncertainty, regularization, and applied modeling theory.

While it is difficult to directly compare 'best fit' models for different experiments, the following observations are robust:

- (i) For the same frequency band S velocity tomography provides higher image resolution than P velocity tomography since the S-wave delays are stronger and S-wave sensitivity zones are smaller.
- (ii) As it accounts for the finite sensitivity zones of waves, finite-frequency inversions provide a clearer and higher-amplitude image of the plume tail than ray-theoretical inversions.

- 532 (iii) Measurements of traveltimes delays of SKS contribute to the imaging of plume tails.
533 This supports the argument by *Wolfe et al.* [2009] that SKS extends tomographic
534 resolving power to deeper depths.
- 535 (iv) The uncertainty in the measured traveltimes delay poses a significant limitation on
536 resolution. When the measurement uncertainty is larger than about 1.0 s, it is equal
537 to or it exceeds the expected delay time imparted by plume tail in the deep man-
538 tle on the S-wave (see Figure 8 in *Maguire et al.* [2016]). In this case, plume tails
539 cannot be resolved. Hence, accurate estimates earthquake hypocenter locations and
540 event origin times and understanding the effects of the crust and shallow mantle on
541 traveltimes are critical to resolving plumes.
- 542 (v) Wide aperture (4,000 – 6,000 km) networks with dense station coverage (< 100 –
543 200 km station spacing) are necessary to image narrow (< 500 km wide) thermal
544 plume tails. Large scale deployments of OBS networks could significantly advance
545 plume imaging.

546 Imaging artifacts appear when data coverage is heterogeneous and the effects of
547 model regularization are relatively large. Due to the predominantly near-vertical wave
548 propagation of teleseismic body waves below a regional network, seismic velocity anoma-
549 lies are artificially elongated in the vertical direction. The artificial elongation bears a
550 strong resemblance to the resolved anomalies in the lower mantle in the shear velocity
551 model of *Wolfe et al.* [2009]. Ring-shaped high-velocities anomalies surrounding the low-
552 velocity plume anomaly are primarily an effect of regularization. Such artifacts can be
553 minimized by carefully balancing smoothness and norm damping parameters.

554 Further modeling work should focus on constraining the effects of compositional
555 variability in plumes on their dynamics and seismic velocity expression, as well as as-
556 sessing travel time delays caused by thermochemical plumes. Additionally, the seismic
557 expression of plumes in whole mantle convection models should be examined.

558 **Acknowledgments**

559 The Computational Infrastructure for Geodynamics provided the code SPECFEM3D-
560 Globe used to compute waveforms. This work is supported by by NSF grants EAR-1246700
561 and EAR-1565511. Computational resources were made available through XSEDE grant
562 TG-EAR15001. We thank two anonymous reviewers and Associate Editor Sebastien Chevrot

563 for helpful reviews. The geodynamic plume models used in our analysis, as well as tables
564 of calculated travel time delays, are available as supplementary data in the online version
565 of this paper.

566 **References**

- 567 Allen, R. M., G. Nolet, W. J. Morgan, K. Vogfjórd, B. H. Bergsson, P. Erlendsson, G. R.
568 Foulger, S. Jakobsdóttir, B. R. Julian, M. Pritchard, S. Ragnarsson, and R. Stefánsson
569 (1999), The thin hot plume beneath Iceland, *Geophysical Journal International*, 137,
570 51–63, doi:10.1046/j.1365-246x.1999.00753.x.
- 571 Ballmer, M., P. E. van Keken, and G. Ito (2015), Hotspots, large igneous provinces, and
572 melting anomalies, in *Treatise on Geophysics (Second Edition)*, edited by G. Schubert,
573 pp. 393 – 459, Elsevier, Oxford, England, doi:https://doi.org/10.1016/B978-0-444-
574 53802-4.00133-0.
- 575 Ballmer, M. D., G. Ito, C. J. Wolfe, and S. C. Solomon (2013), Double layering of a ther-
576 mochemical plume in the upper mantle beneath Hawaii, *Earth and Planetary Science*
577 *Letters*, 376, 155–164, doi:10.1016/j.epsl.2013.06.022.
- 578 Bonnin, M., G. Nolet, A. Villaseñor, J. Gallart, and C. Thomas (2014), Multiple-frequency
579 tomography of the upper mantle beneath the African/Iberian collision zone, *Geophysical*
580 *Journal International*, 198, 1458–1473, doi:10.1093/gji/ggu214.
- 581 Bossmann, A. B., and P. E. van Keken (2013), Dynamics of plumes in a compressible
582 mantle with phase changes: Implications for phase boundary topography, *Physics of the*
583 *Earth and Planetary Interiors*, 224, 21–31, doi:10.1016/j.pepi.2013.09.002.
- 584 Bozdağ, E., D. Peter, M. Lefebvre, D. Komatitsch, J. Tromp, J. Hill, N. Podhorszki, and
585 D. Pugmire (2016), Global adjoint tomography: First-generation model, *Geophysical*
586 *Journal International*, 207(3), 1739–1766, doi:10.1093/gji/ggw356.
- 587 Burdick, S., F. L. Vernon, V. Martynov, J. Eakins, T. Cox, J. Tytell, T. Mulder, M. C.
588 White, L. Astiz, G. L. Pavlis, and R. D. van der Hilst (2017), Model update May
589 2016: upper–mantle heterogeneity beneath North America from travel–time tomogra-
590 phy with global and USArray data, *Seismological Research Letters*, 88, 319–325, doi:
591 10.1785/0220160186.
- 592 Charléty, J., S. Voronin, G. Nolet, I. Loris, F. J. Simons, K. Sigloch, and I. C. Daubechies
593 (2013), Global seismic tomography with sparsity constraints: Comparison with smooth-
594 ing and damping regularization, *Journal of Geophysical Research E: Planets*, 118(9),

4887–4899, doi:10.1002/jgrb.50326.

Chevrot, S., R. Martin, and D. Komatitsch (2012), Optimized discrete wavelet transforms in the cubed sphere with the lifting scheme-implications for global finite-frequency tomography, *Geophysical Journal International*, *191*(3), 1391–1402, doi:10.1111/j.1365-246X.2012.05686.x.

Cobden, L., S. Goes, F. Cammarano, and J. a. D. Connolly (2008), Thermochemical interpretation of one-dimensional seismic reference models for the upper mantle: Evidence for bias due to heterogeneity, *Geophysical Journal International*, *175*(2), 627–648, doi: 10.1111/j.1365-246X.2008.03903.x.

Connolly, J. A. D. (2005), Computation of phase equilibria by linear programming: A tool for geodynamic modeling and its application to subduction zone decarbonation, *Earth and Planetary Science Letters*, *236*, 524–541, doi:10.1016/j.epsl.2005.04.033.

Dahlen, F. A., S.-H. Hung, and G. Nolet (2000), Fréchet kernels for finite-frequency traveltimes—I. Theory, *Geophysical Journal International*, *141*, 157–174, doi: 10.1046/j.1365-246X.2000.00070.x.

Dannberg, J., and S. V. Sobolev (2015), Low-buoyancy thermochemical plumes resolve controversy of classical mantle plume concept, *Nature Communications*, *6*, 6960, doi: 10.1038/ncomms7960.

Dziewonski, A. M., and D. L. Anderson (1981), Preliminary reference Earth model, *Physics of the Earth and Planetary Interiors*, *25*, 297–356, doi:10.1016/0031-9201(81)90046-7.

French, S. W., and B. A. Romanowicz (2015), Broad plumes rooted at the base of the Earth’s mantle beneath major hotspots, *Nature*, *525*, 95–99, doi:10.1038/nature14876.

Gokhberg, A., and A. Fichtner (2016), Full-waveform inversion on heterogeneous HPC systems, *Computers and Geosciences*, *89*, 260–268, doi:10.1016/j.cageo.2015.12.013.

Grand, S. P. (1987), Tomographic inversion for shear velocity beneath the North American plate, *Journal of Geophysical Research*, *92*, 14,065–14,090, doi: 198710.1029/JB092iB13p14065.

Hung, S.-H., F. A. Dahlen, and G. Nolet (2001), Wavefront healing: a banana–doughnut perspective, *Geophysical Journal International*, *146*, 289–312.

Hwang, Y. K., J. Ritsema, P. E. van Keken, S. Goes, and E. E. Styles (2011), Wavefront healing renders deep plumes seismically invisible, *Geophysical Journal International*, *187*, 273–277, doi:10.1111/j.1365-246X.2011.05173.x.

- 628 Kawakatsu, H., G. Ekström, R. Evans, D. Forsyth, J. Gaherty, B. Kennett, J.-P. Montagner,
629 and H. Utada (2016), Pacific array (transportable broadband ocean floor array), in *EGU*
630 *General Assembly Conference Abstracts*, vol. 18, p. 2514.
- 631 Komatitsch, D., and J. Tromp (2002), Spectral-element simulations of global seismic
632 wave propagation-I. Validation, *Geophysical Journal International*, *149*, 390–412, doi:
633 10.1046/j.1365-246X.2002.01653.x.
- 634 Laske, G., J. A. Collins, C. J. Wolfe, S. C. Solomon, R. S. Detrick, J. A. Orcutt,
635 D. Bercovci, and E. H. Hauri (2009), Probing the Hawaiian hot spot with new broad-
636 band ocean bottom instruments, *Eos*, *90*, 362–363, doi:10.1029/2009EO410002.
- 637 Leonard, T., and L. Liu (2016), The role of a mantle plume in the formation of Yellow-
638 stone volcanism, *Geophysical Research Letters*, *43*, 1132–1139.
- 639 Li, X. H., R. Kind, K. Priestley, S. V. Sobolev, F. Tilmann, X. Yuan, and M. Weber
640 (2000), Mapping the Hawaiian plume conduit with converted seismic waves, *Nature*,
641 *405*, 938–941, doi:10.1038/35016054.
- 642 Lin, S.-C., and P. E. van Keken (2006), Dynamics of thermochemical plumes: 1. Plume
643 formation and entrainment of a dense layer, *Geochemistry, Geophysics, Geosystems*, *7*,
644 doi:10.1029/2005GC001071.
- 645 Maguire, R., J. Ritsema, P. E. van Keken, A. Fichtner, and S. Goes (2016), P- and S-wave
646 delays caused by thermal plumes, *Geophysical Journal International*, *206*, 1169–1178,
647 doi:10.1093/gji/ggw187.
- 648 Mercerat, D. E., and G. Nolet (2013), On the linearity of cross-correlation delay times
649 in finite-frequency tomography, *Geophysical Journal International*, *192*, 681–687, doi:
650 10.1093/gji/ggs017.
- 651 Montelli, R., G. Nolet, F. A. Dahlen, G. Masters, E. R. Engdahl, and S.-H. Hung (2004),
652 Finite-frequency tomography reveals a variety of plumes in the mantle., *Science*, *303*,
653 338–343, doi:10.1126/science.1092485.
- 654 Nolet, G., and F. A. Dahlen (2000), Wavefront healing and the evolution of seismic delay
655 times, *Journal of Geophysical Research*, *105*, 19,043–19,504.
- 656 Porritt, R. W., R. M. Allen, and F. F. Pollitz (2014), Seismic imaging east of the Rocky
657 Mountains with USArray, *Earth and Planetary Science Letters*, *402*, 16–25.
- 658 Rickers, F., A. Fichtner, and J. Trampert (2012), Imaging mantle plumes with instan-
659 taneous phase measurements of diffracted waves, *Geophysical Journal International*,
660 *190*(1), 650–664, doi:10.1111/j.1365-246X.2012.05515.x.

- 661 Rickers, F., A. Fichtner, and J. Trampert (2013), The Iceland-Jan Mayen plume sys-
662 tem and its impact on mantle dynamics in the North Atlantic region: Evidence
663 from full-waveform inversion, *Earth and Planetary Science Letters*, 367, 39–51, doi:
664 10.1016/j.epsl.2013.02.022.
- 665 Schmandt, B., and F.-C. Lin (2014), P and S wave tomography of the mantle beneath the
666 United States, *Geophysical Research Letters*, 41, 6342–6349.
- 667 Schmandt, B., K. G. Dueker, E. D. Humphreys, and S. Hansen (2012), Hot mantle up-
668 welling across the 660 beneath Yellowstone, *Earth and Planetary Science Letters*, 331-
669 332, 224–236, doi:10.1016/j.epsl.2012.03.025.
- 670 Shen, Y., S. C. Solomon, I. T. Bjarnason, and C. J. Wolfe (1998), Seismic evidence for a
671 lower-mantle origin of the Iceland mantle plume, *Nature*, 395, 62–65.
- 672 Sigloch, K., N. McQuarrie, and G. Nolet (2008), Two-stage subduction history under
673 North America inferred from multiple-frequency tomography, *Nature Geoscience*, 1(7),
674 458–462, doi:10.1038/ngeo231.
- 675 Sleep, N. H. (1990), Hotspots and mantle plumes: Some phenomenology, *Journal of Geo-*
676 *physical Research*, 95, 6715–6736.
- 677 Spakman, W., S. Stein, R. van der Hilst, and R. Wortel (1989), Resolution experiments for
678 NW Pacific subduction zone tomography, *Geophysical Research Letters*, 16, 1097–1100.
- 679 Stixrude, L., and C. Lithgow-Bertelloni (2011), Thermodynamics of mantle miner-
680 als - II. Phase equilibria, *Geophysical Journal International*, 184, 1180–1213, doi:
681 10.1111/j.1365-246X.2010.04890.x.
- 682 Styles, E. E., S. Goes, P. E. van Keken, J. Ritsema, and H. E. Smith (2011), Syn-
683 thetic images of dynamically predicted plumes and comparison with a global
684 tomographic model, *Earth and Planetary Science Letters*, 311, 351–363, doi:
685 10.1016/j.epsl.2011.09.012.
- 686 Trampert, J., and J. Spetzler (2006), Surface wave tomography: Finite-frequency ef-
687 fects lost in the null space, *Geophysical Journal International*, 164, 394–400, doi:
688 10.1111/j.1365-246X.2006.02864.x.
- 689 Wolfe, C. J., I. T. Bjarnason, J. C. VanDecar, and S. C. Solomon (1997), Seismic structure
690 of the Iceland mantle plume, *Nature*, 385, 245–247, doi:10.1038/385245a0.
- 691 Wolfe, C. J., S. C. Solomon, G. Laske, J. A. Collins, R. S. Detrick, J. A. Orcutt,
692 D. Bercovici, and E. H. Hauri (2009), Mantle shear-wave velocity structure beneath the
693 Hawaiian hot spot., *Science*, 326, 1388–1390, doi:10.1126/science.1180165.

- 694 Workman, R. K., and S. R. Hart (2005), Major and trace element composition of the de-
695pleted MORB mantle (DMM), *Earth and Planetary Science Letters*, *231*, 53–72, doi:
69610.1016/j.epsl.2004.12.005.
- 697 Xue, J., Y. Zhou, and Y. Chen (2015), Tomographic resolution of plume anomalies
698in the lowermost mantle, *Geophysical Journal International*, *201*, 979–995, doi:
69910.1093/gji/ggv067.

Plume	Ra	ΔT_{CMB} (K)	b	Γ_{660} (MPa K ⁻¹)
R1	2×10^6	750	$\ln(10^2)$	-2.5
R2	1×10^6	750	$\ln(10)$	0
R3	8×10^5	550	$\ln(10^3)$	-2.5

700

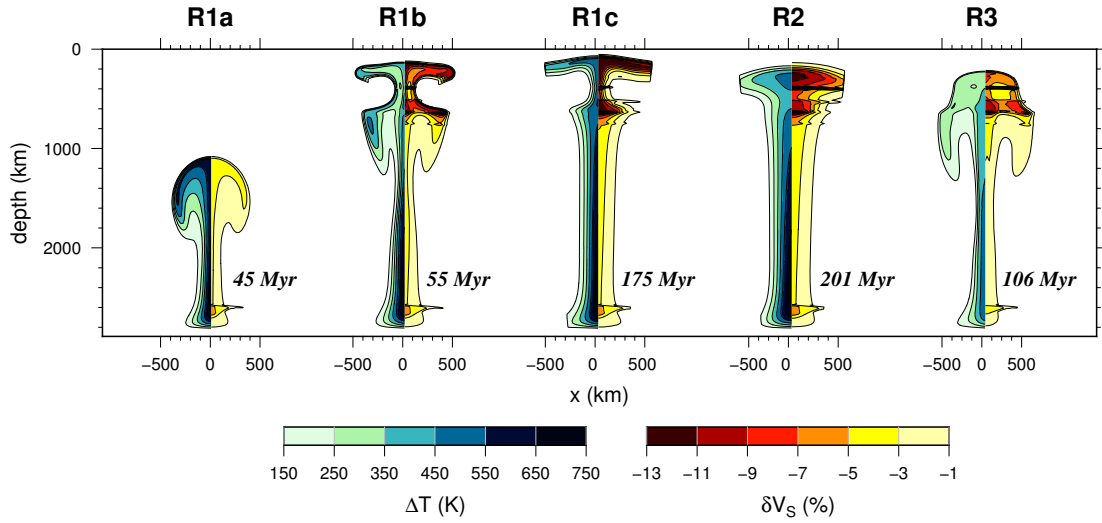
701

702

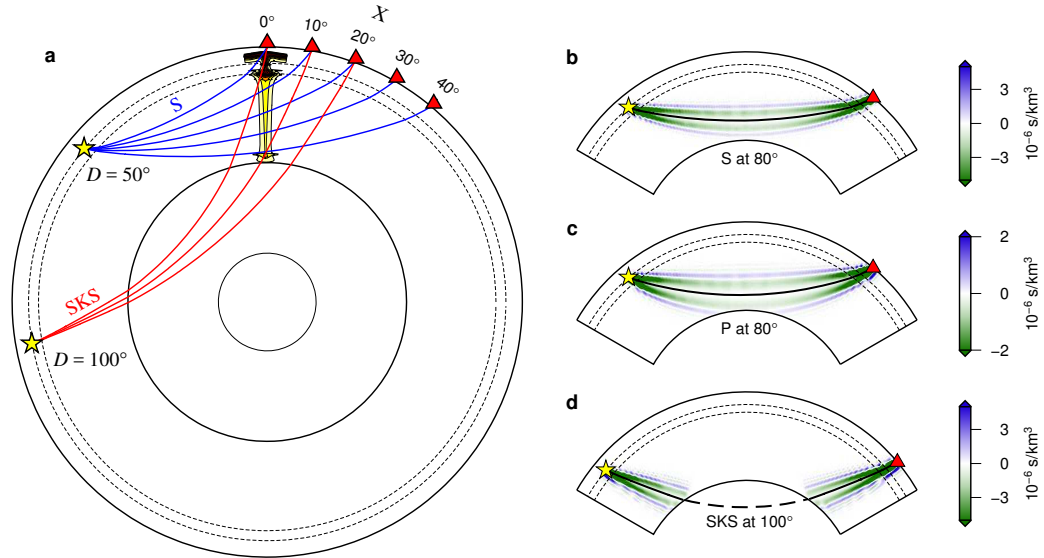
703

704

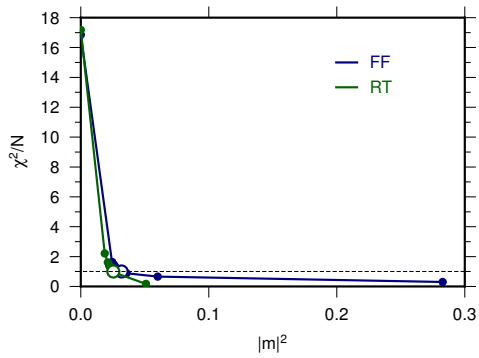
Table 1. Dynamic parameters used in plume simulations. Ra is the thermal Rayleigh number, ΔT_{CMB} is the temperature contrast across the core mantle boundary, b is the temperature dependence of viscosity, and Γ_{660} is the Clapeyron slope of the wadsleyite–bridgmanite phase transition.



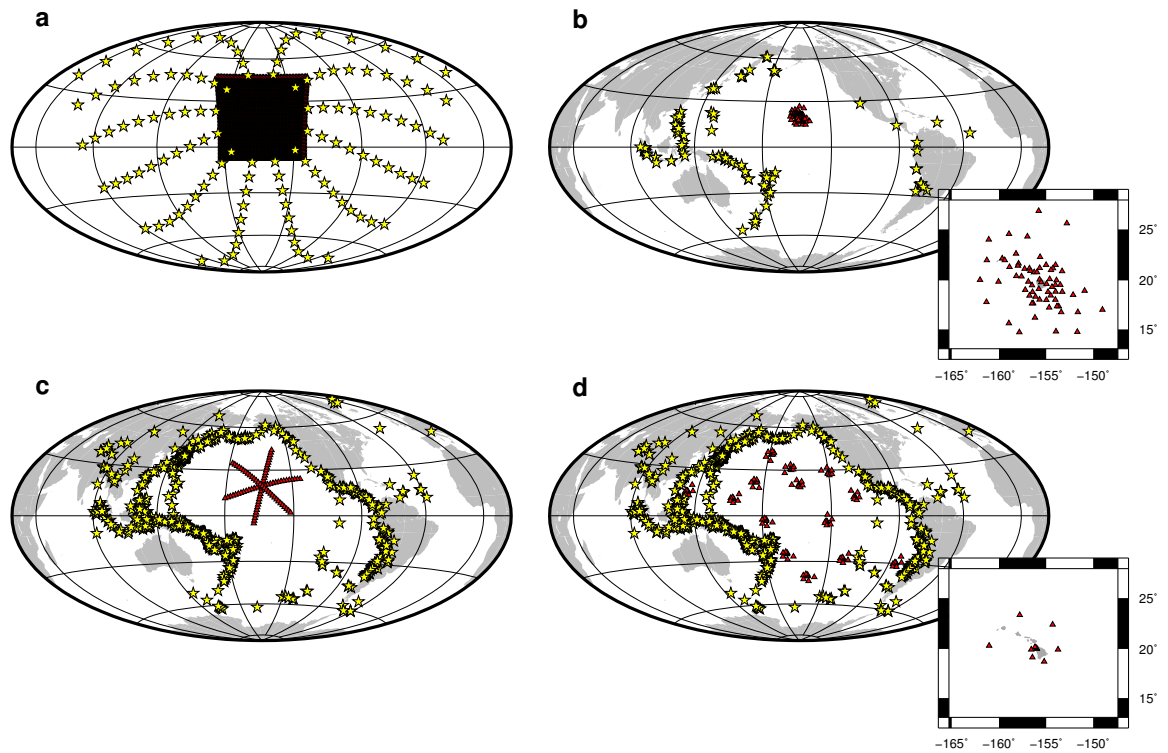
705 **Figure 1.** Dynamic simulations of plumes used in sensitivity tests. The plumes are symmetric about the
 706 vertical axis at $x = 0$. For each plume, the excess temperature is shown on the left and the reduction in shear
 707 velocity δV_S relative to PREM is shown on the right. The plume structures R1a, R1b, and R1c are snapshots
 708 of the same dynamic simulation at 45 Myr, 55 Myr, and 175 Myr, respectively.



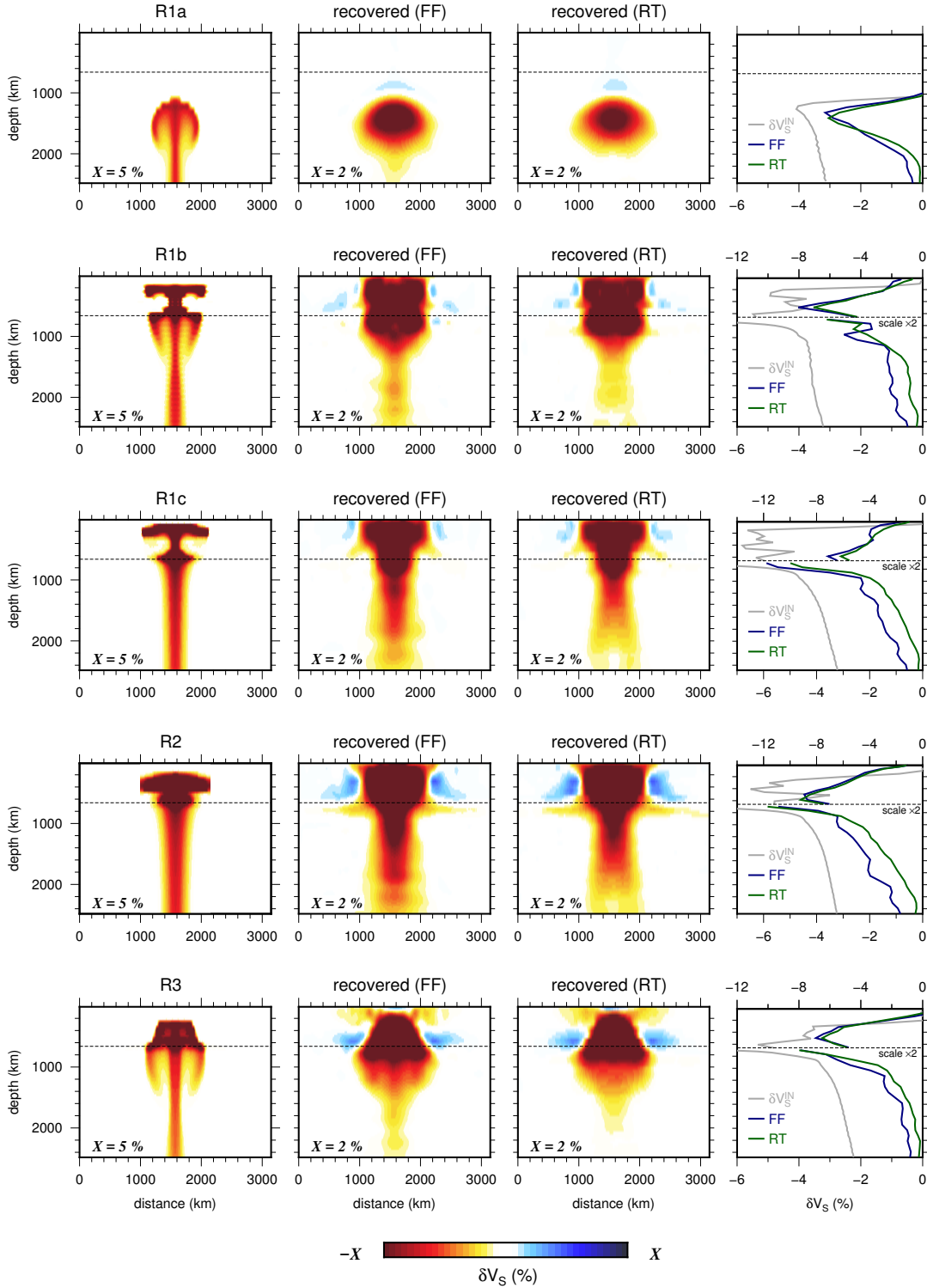
709 **Figure 2.** (a) Ray geometry for S (in blue) and SKS (in red) waves traversing plume R1c. The distance D
 710 between the earthquake and plume is 50° for S and 100° for SKS. X is the angular distance beyond the plume
 711 along the great circle path. (b – d) Sensitivity kernels $K(x)$ for cross correlation travel time delays measured
 712 over the frequency band 0.04 – 0.10 Hz. Kernels are shown for an S-wave at an epicentral distance of 80° (in
 713 b), a P-wave at 80° (in c), and an SKS-wave at an epicentral distance of 100° (in d). The yellow star indicates
 714 the earthquake and the red triangle indicates the receiver. Earthquakes are 400 km deep. The black lines in
 715 the center of the kernels are the geometric ray paths.



716 **Figure 3.** The tradeoff curve of misfit versus model norm obtained for plume R1a using network configu-
 717 ration A (see section 3.1). Results for FF are shown in blue and results of RT are shown in green. The open
 718 circles indicate the 'best' model, for which the model fits the data to within uncertainty (i.e., $\chi^2 = N$). The
 719 best model \mathbf{m} is smaller for RT than FF for a given misfit χ^2 .



720 **Figure 4.** Source–receiver geometries used in synthetic tomography experiments. Yellow stars indicate
 721 earthquakes and red triangles indicate receivers. (a) represents a scenario in which earthquakes are recorded
 722 on a rectangular network at distances D between 30° and 120° and with uniform azimuthal coverage. The
 723 width L of the network is 6,000 km, and the spacing between stations Δx is 100 km. The network geometry
 724 shown in (b) is identical to the PLUME geometry [Wolfe *et al.*, 2009]. The earthquakes are larger than mag-
 725 nitude 6 between 2012 and 2017. Panels (c) and (d) illustrate hypothetical deployments in the Pacific Ocean.
 726 The earthquake locations are taken from the historical seismicity record of events greater than M_W 6 over
 727 the previous five years. The network in (c) comprises three intersecting linear arrays with $\Delta x = 200$ km. The
 728 arrays-of-arrays network shown in (d) is similar to the proposed Pacific Array.

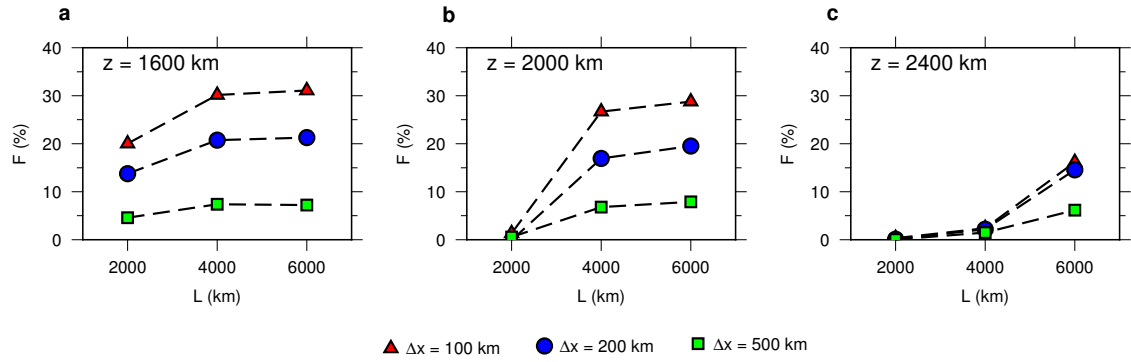


729 **Figure 5.** Shear velocity structures of the plumes R1, R2, and R3 obtained by inverting S-wave delay times
 730 for network geometry A (Figure 4a) with $L = 6,000$ km, $\Delta x = 100$ km. The standard deviation of the travel-

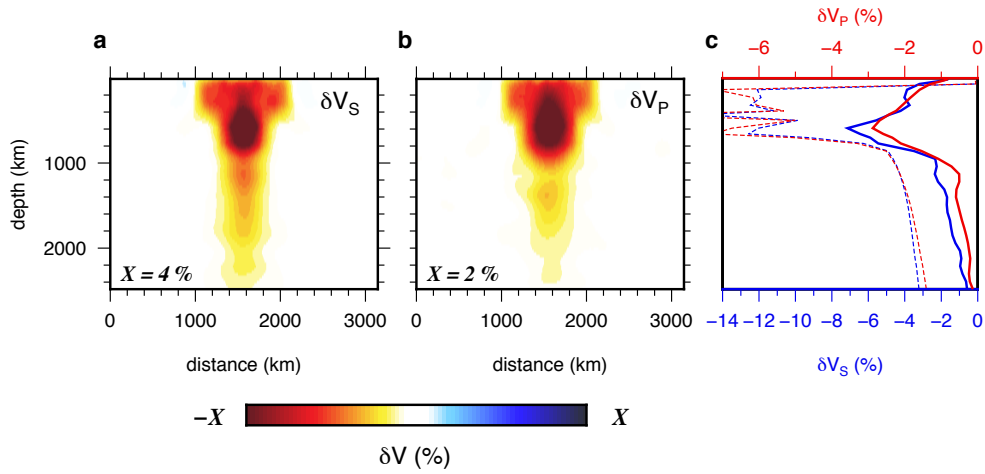
731 time uncertainty is $\sigma = 0.1$ s. The first column shows the structures of the input plume models. The second
 732 and third columns show the resolved velocity structures using FF and RT, respectively. The dotted line is the

660 discontinuity. This article is protected by copyright. All rights reserved.

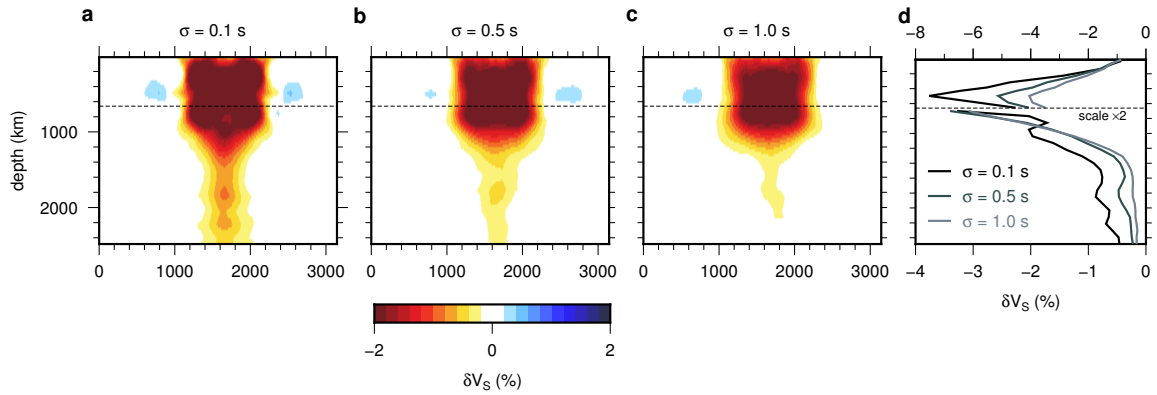
734 The anomalies below



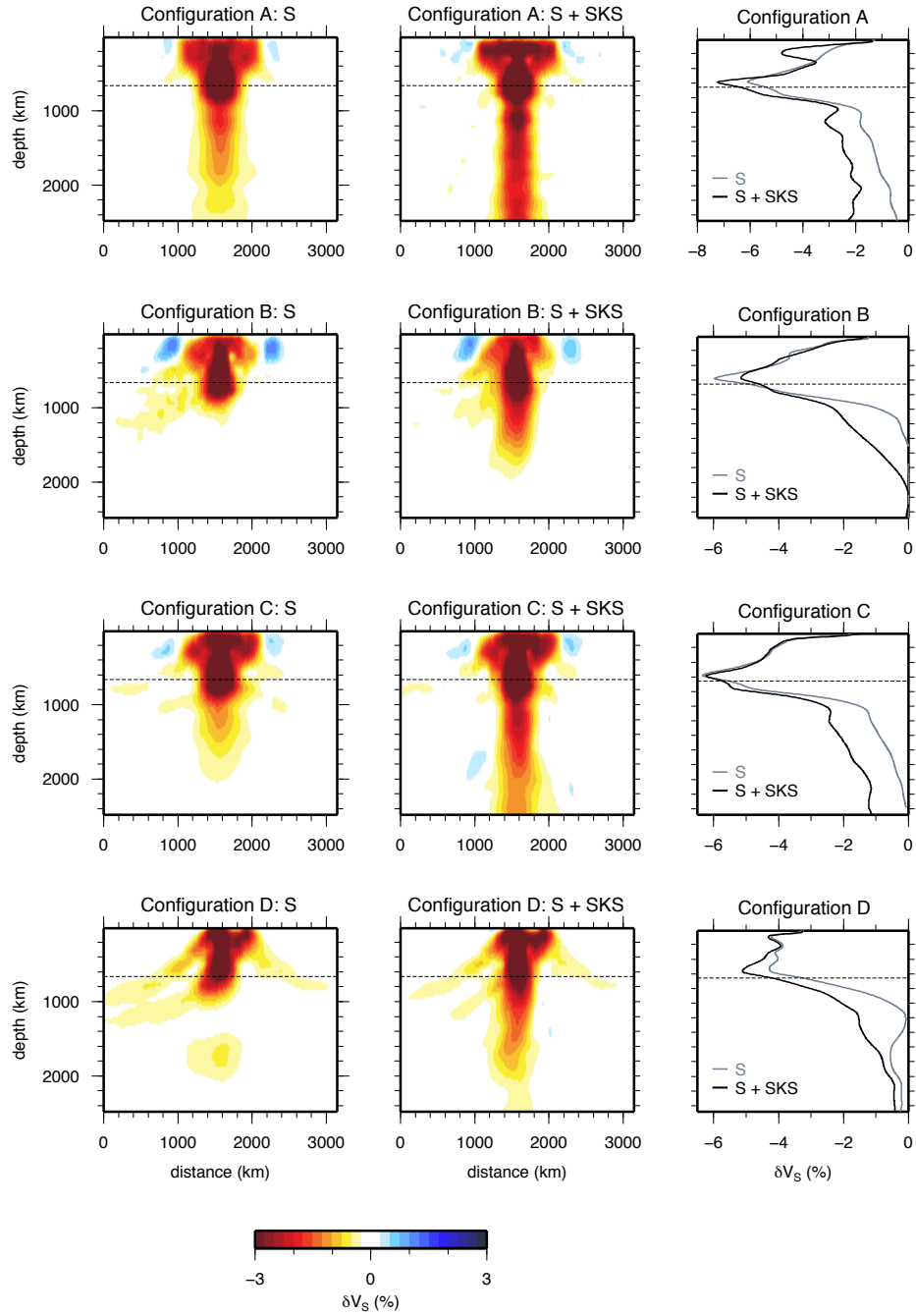
736 **Figure 6.** The fraction F recovered of the velocity anomaly within the tail of R1b as a function of net-
 737 work width L . F is determined for a station spacing Δx of 100 km (triangles), 200 km (circles), and 500 km
 738 (squares) and for three depths along the plume axis: (a) 1,600 km, (b) 2,000 km, and (c) 2,400 km. Delay
 739 times are inverted using FF.



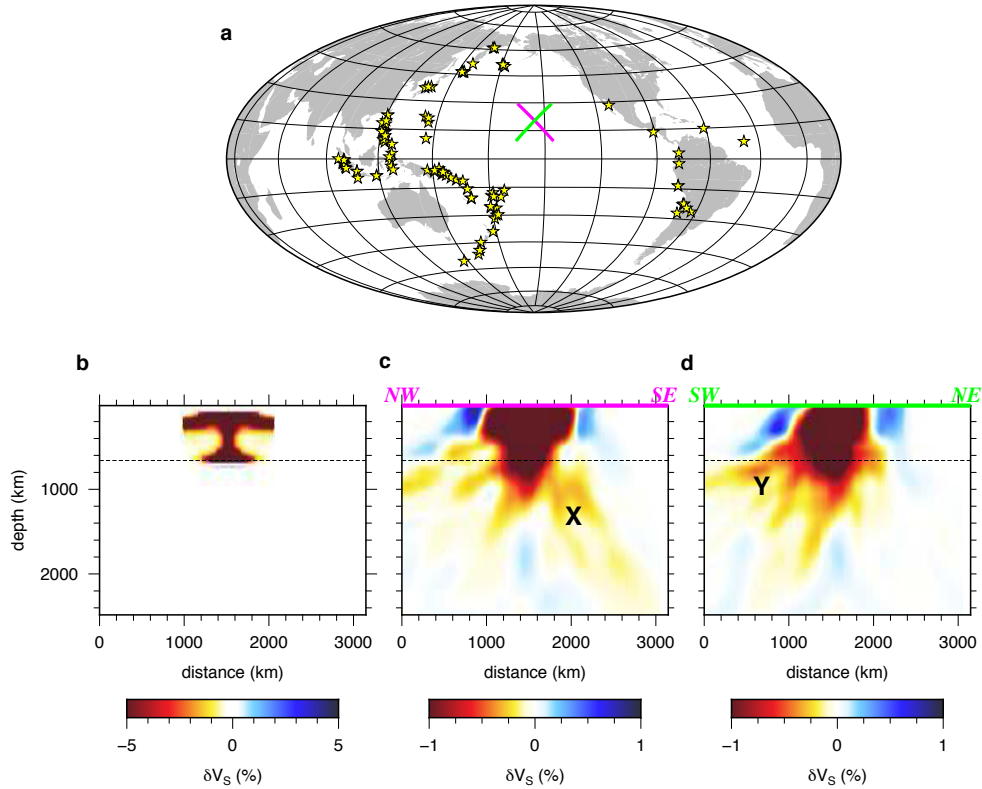
740 **Figure 7.** Comparison of (a) the resolved S-wave velocity δV_S and (b) the resolved P-wave velocity δV_P
 741 structures for plume R1c using the idealized source–receiver geometry and FF theory. The scale X of the
 742 colorbar is indicated in the lower left corner. c) shows δV_S (blue) and δV_P (red) along the plume axis. Dashed
 743 lines indicate the axial anomaly of the input model.



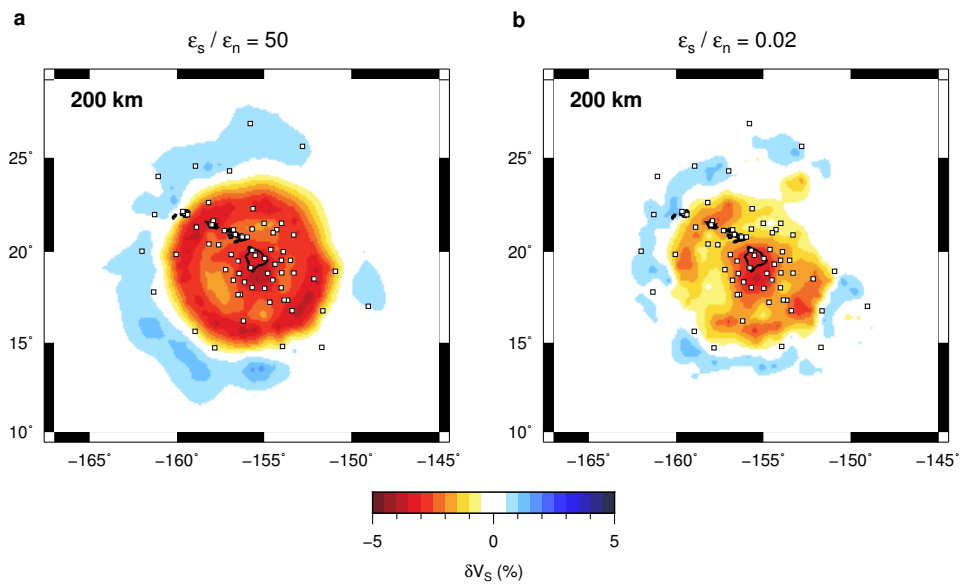
744 **Figure 8.** Effect of Gaussian noise in the travelt ime measurements on tomographic imaging of plumes
 745 using FF and S travelt ime delays. Panels (a), (b), and (c) show FF S-wave inversion results of R1b, with dif-
 746 ferent values for the standard deviation of Gaussian noise σ . Panel (d) shows the structure of each of the three
 747 models along the plume axis. The scale of the x-axis is enlarged by a factor of two in the lower mantle.



748 **Figure 9.** Inversions of R1c for all source-receiver configurations using FF. The rows correspond to i) the
 749 idealized rectangular grid ii) the PLUME geometry iii) the intersecting linear arrays and iv) the Pacific array.
 750 Models in the left column use only S traveltimes and models in the middle column use S and SKS traveltimes.
 751 The right column compares inversion results for S and S+SKS along the plume axis.



752 **Figure 10.** Smearing test for the PLUME experiment (i.e., configuration B). S and SKS traveltimes are
 753 jointly inverted using FF. a) Earthquake distribution used in the inversion, as well as the locations of cross
 754 sections through recovered model. b) Input plume structure, which is the upper mantle expression of R1c
 755 (i.e., R1c where the plume tail has been artificially removed). c) NW–SE cross section through the recovered
 756 model. The feature labeled 'X' illustrates smearing oriented steeply to the SE due to the prevailing incom-
 757 ing ray direction of South American events. d) SW–NE cross section through recovered model. The feature
 758 labeled 'Y' reflects smearing to the SW owing to the prevalence of South Pacific events.



759 **Figure 11.** Effect of regularization parameters. Inversions shown are for R1b using S and SKS travel times,
760 and the PLUME geometry. Horizontal slices of the model are taken at 200 km depth. In (a) smooth models
761 are preferred ($\epsilon_s / \epsilon_n = 50$), and in (b) small models are preferred ($\epsilon_s / \epsilon_n = 0.02$).

Figure 1.

Author Manuscript

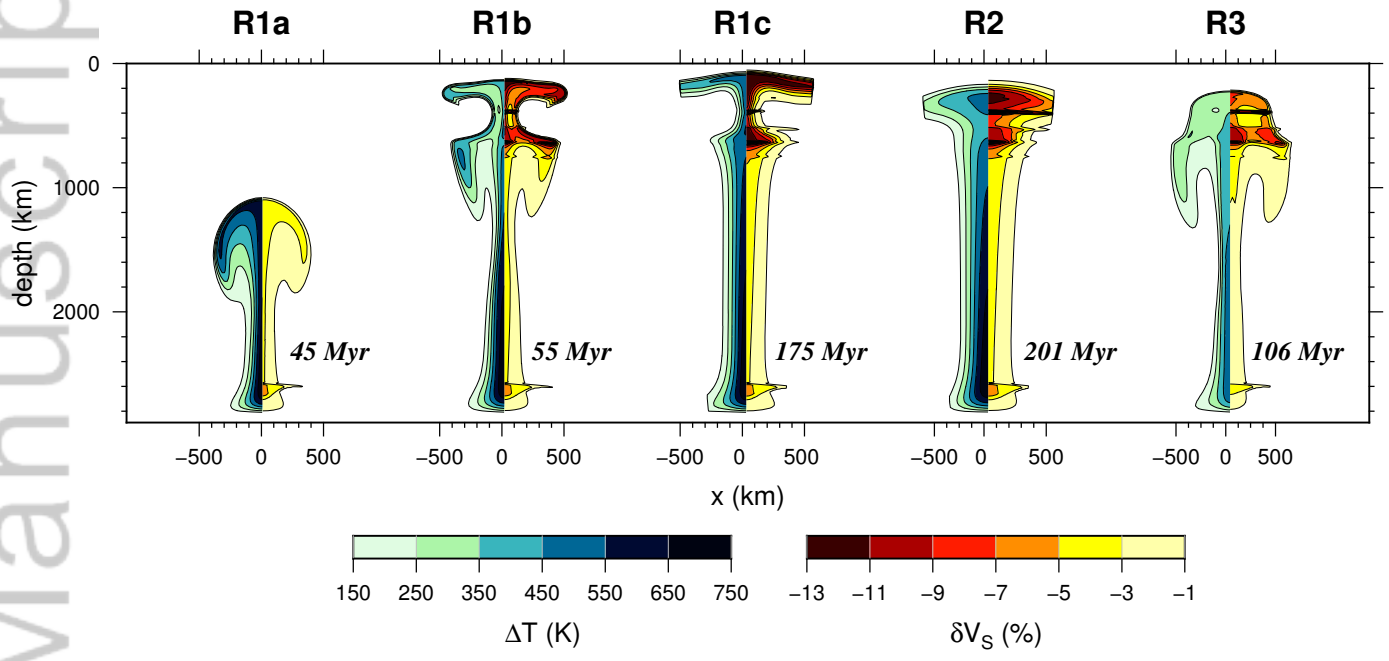


Figure 2.

Author Manuscript

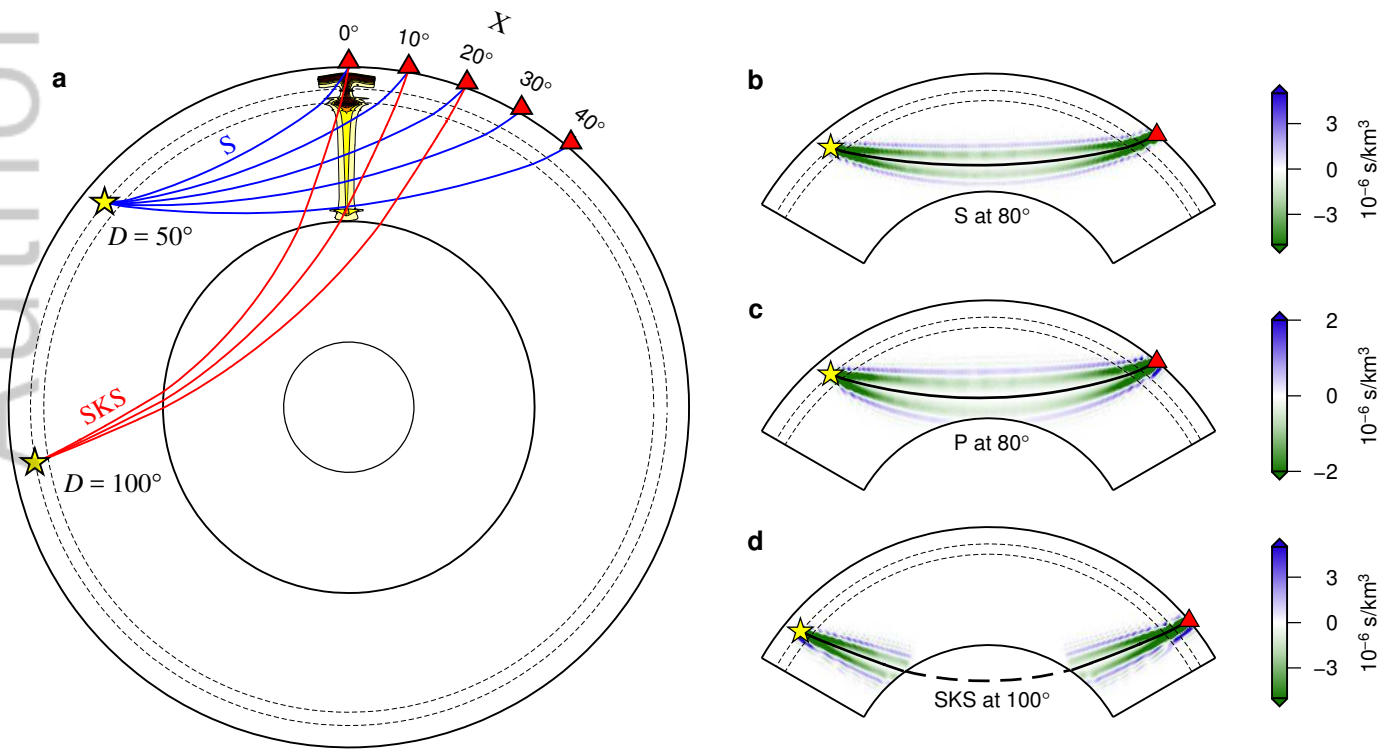


Figure 3.

Author Manuscript

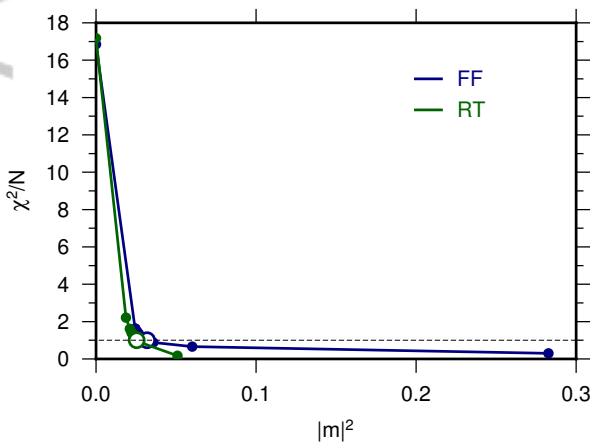


Figure 4.

Author Manuscript

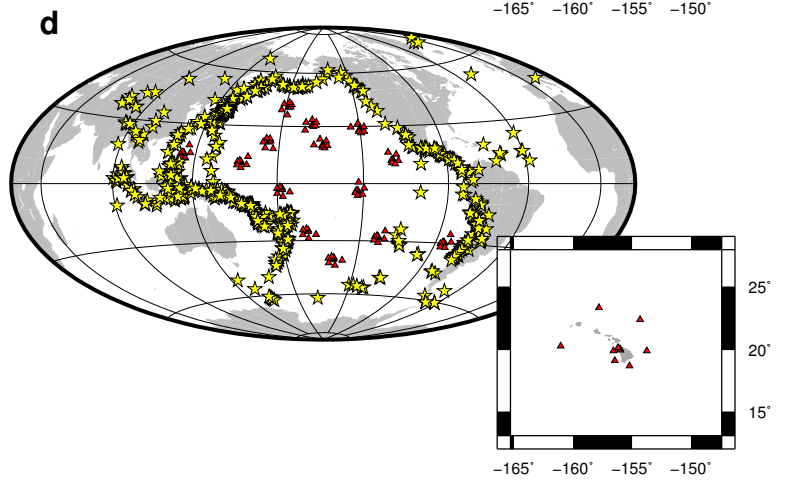
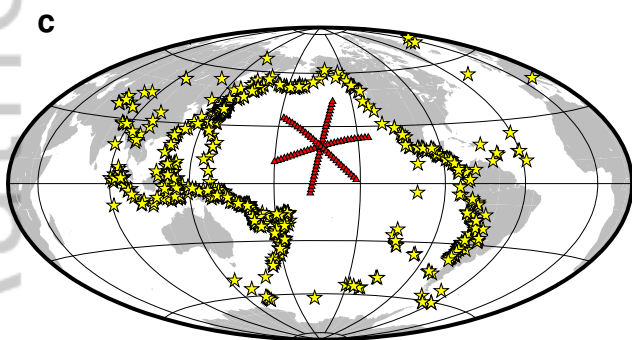
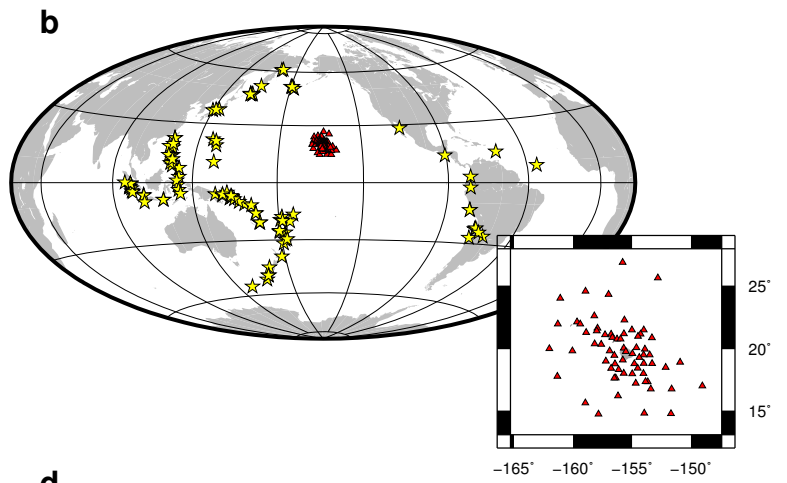
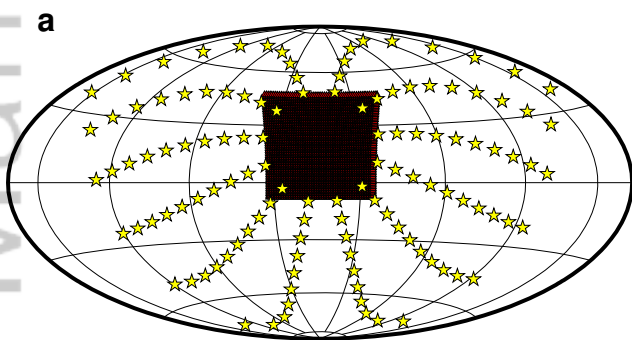


Figure 5.

Author Manuscript

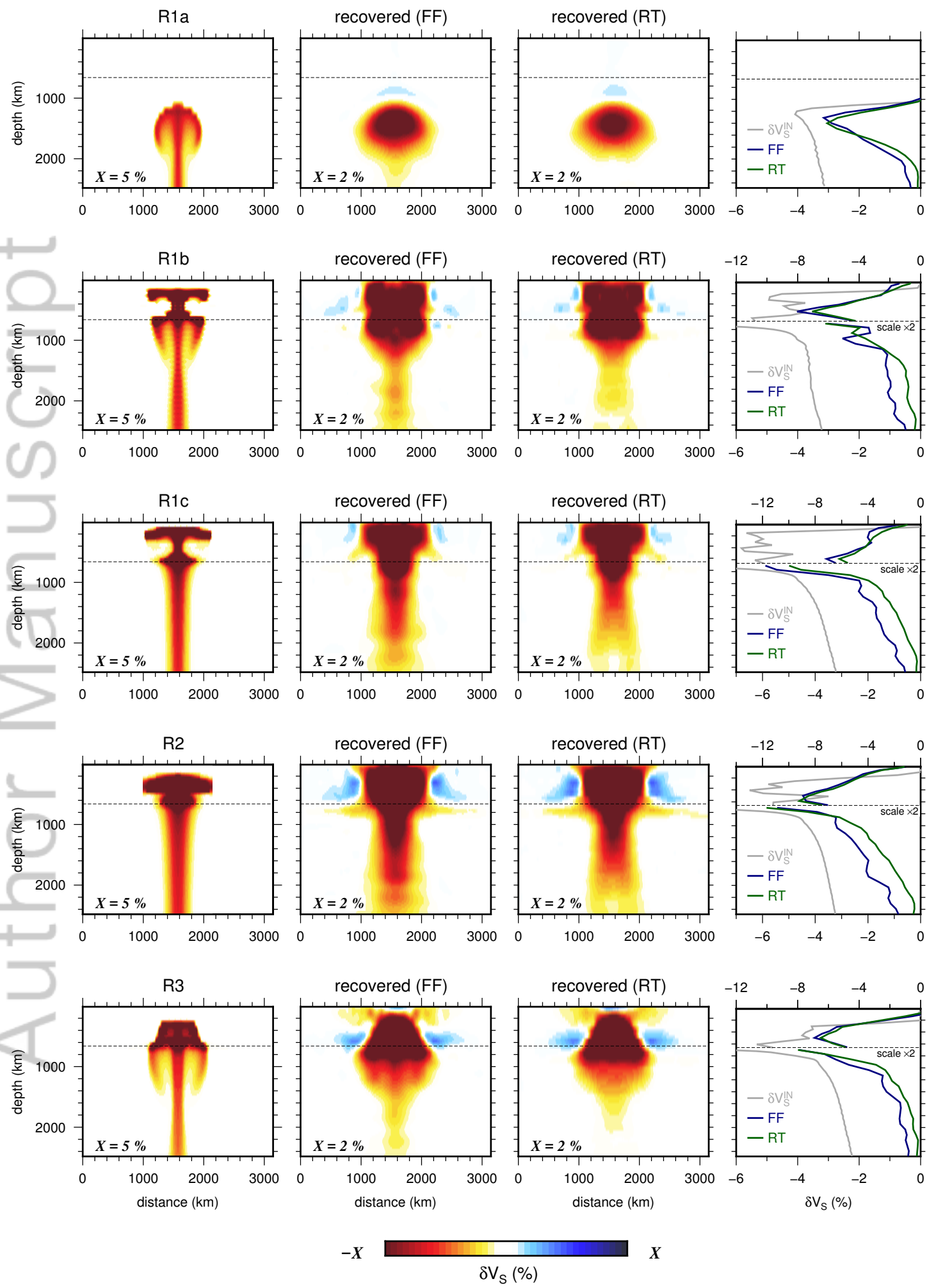


Figure 6.

Author Manuscript

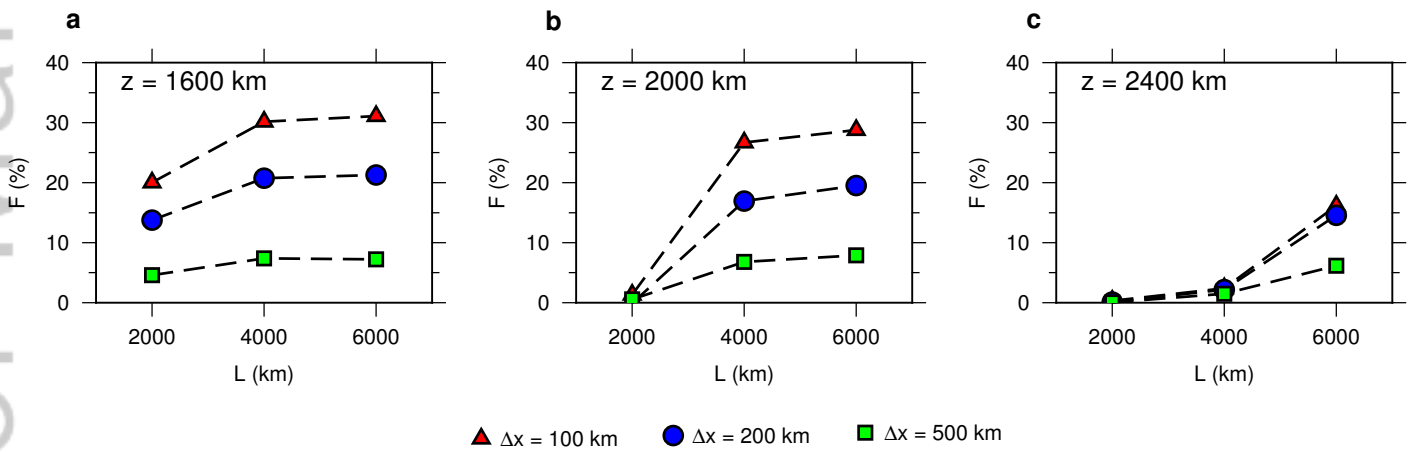


Figure 7.

Author Manuscript

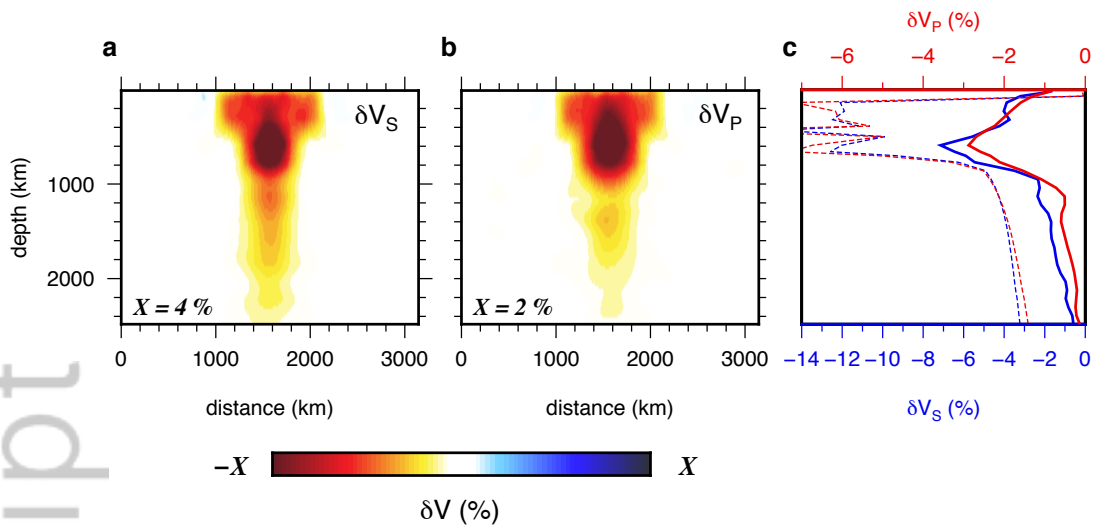


Figure 8.

Author Manuscript

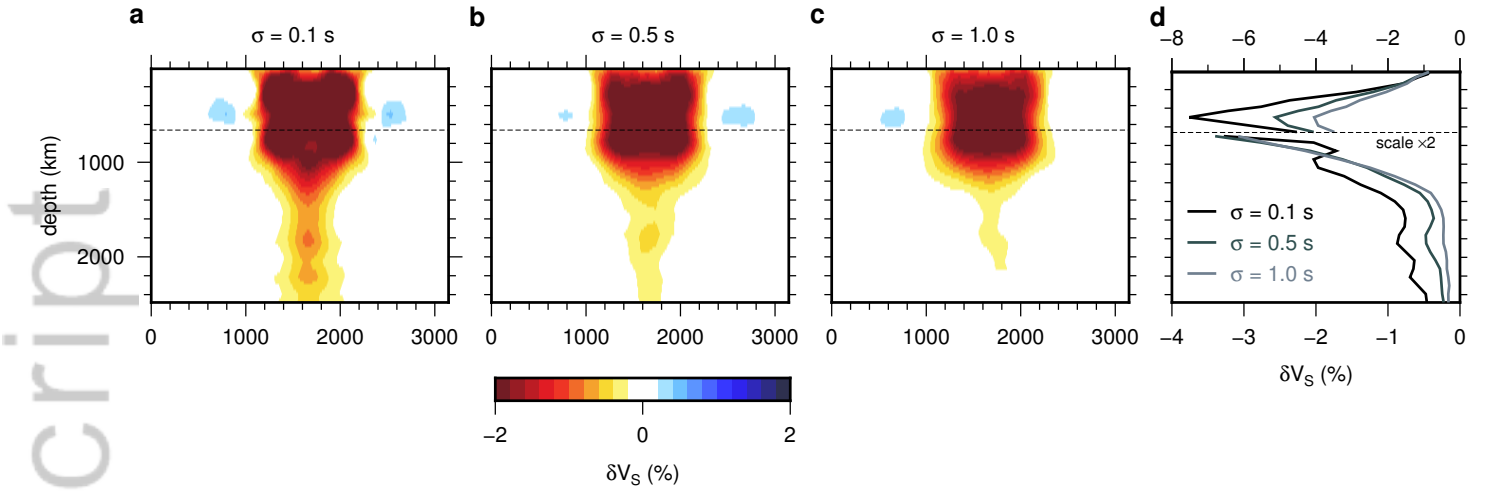


Figure 9.

Author Manuscript

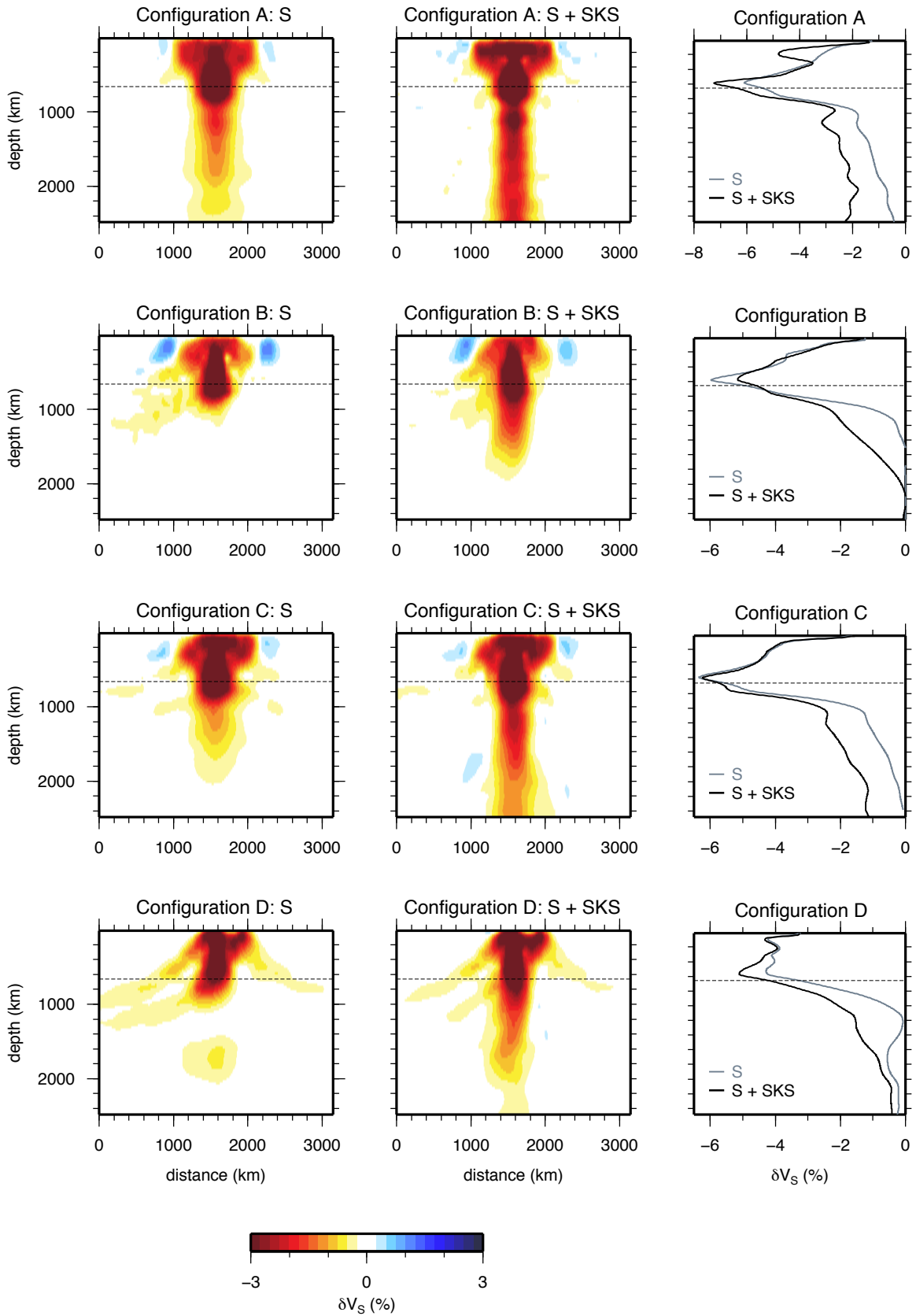


Figure 10.

Author Manuscript

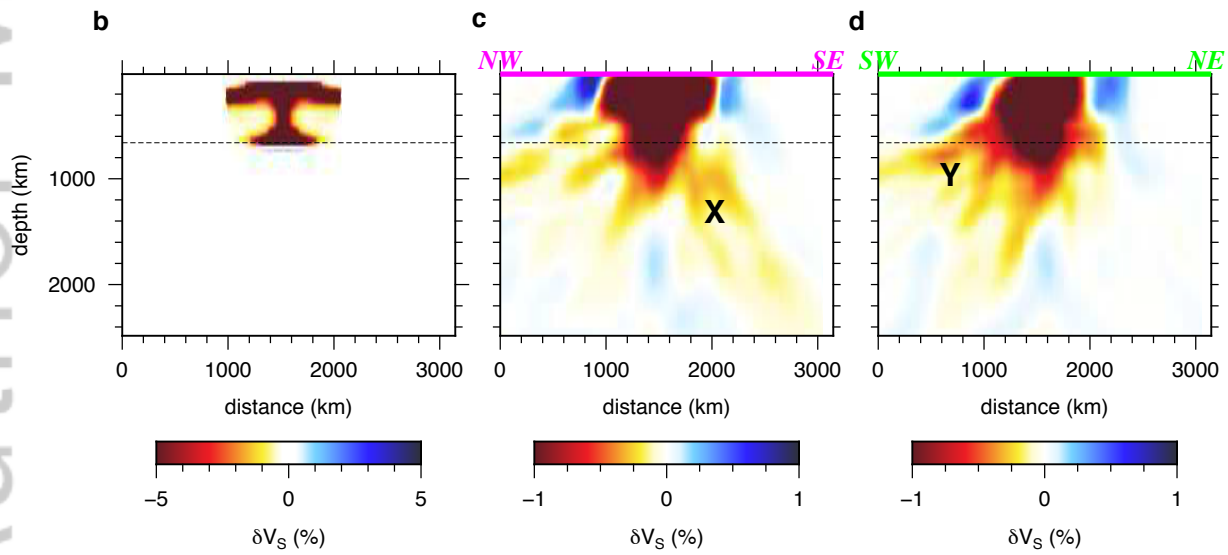
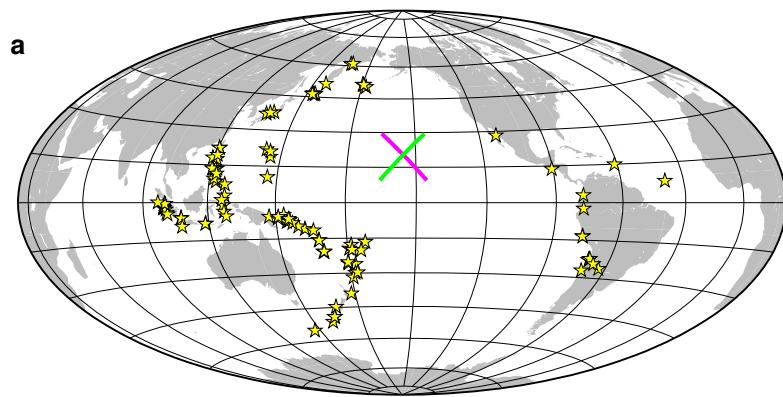


Figure 11.

Author Manuscript

